Visualisation of flooding along an unvegetated, ephemeral river using Google Earth Engine

Li, Jiaguang; Tooth, Stephen; Zhang, Kun; Zhao, Yang

Published in:
Journal of Environmental Management

DOI:
10.1016/j.jenvman.2020.111559

Publication date:
2021

Citation for published version (APA):
Li, J., Tooth, S., Zhang, K., & Zhao, Y. (2021). Visualisation of flooding along an unvegetated, ephemeral river using Google Earth Engine: Implications for assessment of channel-floodplain dynamics in a time of rapid environmental change. *Journal of Environmental Management*, *278*, [111559]. https://doi.org/10.1016/j.jenvman.2020.111559

Visualisation of flooding along an unvegetated, ephemeral river using Google Earth Engine: implications for assessment of channel-floodplain dynamics in a time of rapid environmental change

Jiaguang Li[1*,2], Stephen Tooth[3], Kun Zhang[4], Yang Zhao[1]

1 Key Laboratory of Tectonics and Petroleum Resources of the Ministry of Education, China University of Geosciences, Wuhan, 430074, China

2 Key Laboratory of Theory and Technology of Petroleum Exploration and Development in Hubei Province, Wuhan 430074, China

3 Department of Geography and Earth Sciences, Aberystwyth University, Aberystwyth, SY23 3DB, UK

4 Institute of Geological Survey of Qinghai Province, Xining, 810012, China

Correspondence: Key Laboratory of Tectonics and Petroleum Resources of the Ministry of Education, China University of Geosciences, Wuhan, 430074, China

Tel.: +86 27 67883067 fax: +86 27 67883051

E-mail address: jiaguangli@cug.edu.cn, jiaguangli@gmail.com (J. Li)

Abstract

Given rapid environmental change, the development of new, data-driven, interdisciplinary approaches is essential for improving assessment and management of river systems, especially with respect to flooding. In the world's extensive drylands, difficulties in obtaining field observations of major hydrological events mean that remote sensing techniques are commonly used to map river floods and assess flood impacts. Such techniques, however, are dependent on available cloud-free imagery during or immediately after peak discharge, and single images may omit important flood-related hydrogeomorphological events. Here, we combine multiple Landsat images from Google Earth Engine (GEE) with precipitation datasets and high-resolution (<0.65 m) satellite imagery to visualise flooding and assess the associated channel-floodplain dynamics along a 25 km reach of the unvegetated, ephemeral Río Colorado, Bolivia. After cloud and shadow removal, Landsat surface reflectance data were used to calculate the Modified Normalized Difference Water Index (MNDWI) and map flood extents and patterns. From 2004 through 2016, annual flooding area along the narrow (<30 m), shallow (<1.7 m), fine-grained (dominantly silt/clay) channels was positively correlated (R^2 = 0.83) with 2-day maximum precipitation totals. Rapid meander bend migration, bank erosion, and frequent overbank flooding was associated with formation of crevasse channels, splays, and headward-eroding channels, and with avulsion (shifting of flow from one channel to another). These processes demonstrate ongoing, widespread channel-floodplain dynamics despite low stream powers and cohesive sediments. Application of our study approaches to other dryland rivers will help generate comparative data on the controls, rates, patterns and timescales of channel-floodplain dynamics under scenarios of climate change and direct human impacts, with potential implications for improved river management.

Keywords: channel dynamics, flood mapping, floodplain, Google Earth Engine, meandering river, unvegetated channel

1. Introduction

Despite modest progress in brokering international climate governance frameworks (e.g. Paris Agreement), concern is growing over the likelihood of a global average temperature rise of greater than 1.5 °C by the end of the 21st century (IPCC, 2014; Hoegh-Guldberg et al., 2018). Consequently, major changes to weather- and climate-related phenomena are likely to occur within the next few generations, which will pose considerable challenges for the maintenance or enhancement of environmental, economic and social resilience. To meet these challenges, new, data-driven, interdisciplinary approaches to enable improved assessment of environmental system dynamics are urgently needed, particularly where there is potential for application in management contexts.

Rivers are key environmental systems, playing a crucial role in fluxes and stores of water, sediment and nutrients on local, regional and global scales. In many global regions, however, increased atmospheric warming and various human activities (e.g. land use changes, river damming, flow abstraction) are resulting in profound alterations to the hydrological cycle, including changes to precipitation intensities, river flow variability, and groundwater volumes (Gleeson et al., 2020). Such profound hydrological alterations are commonly manifest in shifts in river flood frequency and magnitude (Woodward et al., 2010), with potential consequences for wider river system structure and function. For instance, within-channel and overbank flooding is a key control on river dynamics, including channel and floodplain stability and the distribution of transported sediment (Nicholas and Walling, 1997; Carroll et al., 2004), and also influences many other aspects of ecosystem service delivery such as riparian biodiversity (Millennium Ecosystem Assessment, 2005). Shifts in flood frequency and magnitude may also pose significant hazards, including by facilitating the spread of water-associated diseases and by impacting on human land use, infrastructure, property, and even life (e.g. Hooke, 2000, 2016; Foody et al., 2004; Ashley and Ashley, 2008; Woodward et al., 2010; Smith et al., 2013; Heaney et al., 2019).

The positive and negative impacts of flooding can affect perennial, humid or tropical region rivers as well as the more commonly intermittent (seasonal) or ephemeral, dryland rivers but accurate mapping and monitoring of flood extents, flood patterns, and associated channel-floodplain dynamics is challenging (Domeneghetti et al., 2019). The challenges are particularly acute in remote, sparsely populated drylands where channel flow gauges are commonly absent or difficult to maintain, and/or field access is often limited during and immediately after the typically irregular flood events (Tooth, 2013; Heritage et al., 2019).

Owing to the difficulties of obtaining field measurements or observations of large or extreme hydrological events in drylands, particular interest has been turning to the use of remote sensing techniques to visualise flooding extent, flooding patterns, and channel-floodplain dynamics along dryland rivers (e.g. Gumbricht et al., 2004; Ip et al., 2006; Milzow et al., 2009; Rowberry et al., 2011; Li et al., 2014a, b, 2018; Thito et al., 2016; Milan et al., 2018; Heritage et al., 2019). Many previous studies have focused on flood mapping from one or a few satellite images captured during or after floods, but these images may contain limited information due to low spectral and temporal resolution (e.g. acquisition dates of satellite imagery long after peak flood events - Ticehurst et al., 2014). In addition, in some dryland regions, obtaining cloud-free imagery during or immediately following peak flood events is notoriously difficult (e.g. Rowberry et al., 2011; Li et al., 2018), and this problem is compounded when attempting to undertake multiple-year mapping and monitoring. Therefore, visualisations of flood extents and patterns remain particularly poorly developed in many drylands. Here, we investigate possible solutions to this problem by using the Google Earth Engine (GEE) platform. The cloud-based GEE platform provides access to worldwide Landsat satellite imagery and has proven computationally efficient for processing large volumes of remote sensing data (Gorelick et al., 2017). In particular, GEE enables all available imagery for a given rainy season to be integrated into one composite, thereby maximizing the accuracy of flood mapping. A number of studies have used GEE to compile composite images and undertake time series analyses, including mapping global water body occurrence and dynamics (Pekel et al., 2016) and assessing monthly changes to water body surface areas (Yang et al., 2020a). Other studies have demonstrated how composite images from GEE enable robust flood monitoring and increased accuracy of flood mapping (Clement et al., 2018; Uddin et al., 2019; DeVries et al., 2020).

In this study, we focus on a 25 km long reach of the unvegetated, ephemeral Río Colorado approaching its terminus on the margins of Salar de Uyuni, Bolivia, the world's largest salt lake (Fig. 1). We generate time-series maps (2004 through 2016) of flood extent and flood patterns. We then combine these maps with other datasets (precipitation measurements, higher resolution satellite imagery) to investigate the controls and consequences of flooding over this time period, especially the associated channel-floodplain dynamics. While the value of GEE-based visualisation and quantification of global water bodies and flooding has been amply demonstrated (Pekel et al., 2016; Yang et al., 2002a; Clement et al., 2018; Uddin et al., 2019; DeVries et al., 2020), until now the approach has not been widely applied for detailed flood mapping and associated analyses of channel-floodplain dynamics along unvegetated, ephemeral rivers.

Reaches of the middle and lower Río Colorado, as well as the neighbouring Río Capilla, have been subject to previous hydrological, geomorphological and sedimentological investigations (e.g. Donselaar et al., 2013; Li et al., 2014a, 2014b, 2015, 2018, 2019, 2020, 2021; Li and Bristow, 2015; van

Toorenenburg et al., 2018). Similar to some other dryland river systems worldwide (e.g. Ielpi, 2018; Ielpi and Lapôtre, 2019), the net moisture deficit and highly saline setting means that these middle and lower reaches are essentially devoid of vegetation cover. Frequent rainfall-flooding events have been shown to be triggers for widespread, pronounced and rapid cascades of channel and floodplain dynamics on (sub-)decadal timescales (e.g. Li et al., 2019, 2020), including meander bend migration and cutoff, crevasse channel and splay formation, and avulsion (defined as the shifting of flow from one channel to another). These previous studies, however, have not generated multi-year flood visualisations or comprehensively investigated the consequences of this flooding for channel-floodplain dynamics.

The specific objectives of this paper thus are to: 1) integrate Landsat data (cloud cover <10%) available for the rainy season of each year from 2004 through 2016 into composite images, and then map flooding extent and pattern using the Modified Normalized Difference Water Index (MNDWI); 2) analyse available precipitation datasets to investigate the relationship between short-term precipitation totals and flooding; 3) use higher resolution satellite imagery to characterize and explain the response of the Río Colorado channels and floodplain to the flooding; and 4) discuss the wider applicability of these data-driven, remote sensing-based approaches for improving assessment and management of a wider diversity of dryland rivers.

2. Study area

The Río Colorado catchment is located in the southern Altiplano basin in the central Andes of South America (Fig. 1a-b). The Altiplano basin formed as part of the Andean oceanic-continental convergent margin and is characterized by an overall semiarid climate, with a marked pattern of increasing aridity from north to south owing to the prevailing low pressure weather systems and poleward low-level airflow (Lenters and Cook, 1999).

The Río Colorado catchment comprises upper Ordivician to Tertiary clastic sedimentary and igneous rocks, with Quaternary sediments widespread (Horton and Decelles, 2001; Marshall et al., 1992). The study area has been tectonically quiescent in the late Pleistocene and Holocene, despite the presence of some prominent fault escarpments in the catchment (Bills et al., 1994; Baucom and Rigsby, 1999; Donselaar et al., 2013; Rigsby et al., 2005). The river flows in a south-north direction, and in the lower reaches develops a fan-shaped form as it approaches its terminus on the southeastern margin of Salar de Uyuni (Fig. 1b). Previous studies have tended to focus on these fan-shaped, lower reaches (e.g. Donselaar et al., 2013; Li et al., 2014a, b, 2015b, 2018; Li and Bristow, 2015; van Toorenenburg et al., 2018) but in this study, the main focus is on a reach of the Río Colorado located 25 to 50 km upstream of the river terminus (Fig. 1c). The distribution of numerous active, abandoning and abandoned channels (Fig. 1c) indicates that this low gradient reach (mean valley gradient ~0.000232 m/m – Fig. 1f) has been subject to repeated avulsions over the last few hundred to few thousand years; during an avulsion, flow is diverted from an active channel and erodes a newer channel on the floodplain and/or reoccupies an older channel, processes that lead to gradual abandonment of the originally active channel (Slingerland and Smith, 2004). In the study reach, two main 'reach-scale' avulsions have occurred since the 1970s, with reaches A-B initially forming the trunk channel, then reaches C-D, and then reaches C-B (Fig. 1c – see also Li et al., 2020). During this time period, 'local-scale' avulsions have also occurred within reach D (Fig. 1d-e). Currently, reach A is abandoned and three principal channels are present (Fig. 1c): the trunk channel (reaches C-B) and two secondary channels (D1, D2). Given the different levels of recent and contemporary activity in these reaches, in this study, we focused mainly on reaches B-D (see Table

1 for a summary of the typical channel and floodplain characteristics). Normalized Difference Vegetation Index (NDVI) analysis (Li et al., 2015a) and field observations demonstrate that the middle and lower reaches of the Río Colorado are essentially unvegetated (Fig. 2).

The study area is influenced by the El Niño-Southern Oscillation (ENSO), with episodic La Niña conditions associated with phases of enhanced rainfall and flooding. Although highly variable, average annual rainfall in the study area is ~185 mm and is greatly exceeded by the annual potential evapotranspiration of 1500 mm. Most precipitation occurs as a consequence of thunderstorms in the rainy season that lasts from December through March (Li et al., 2014a). Daily maximum precipitation totals can represent a significant percentage of the annual total but only rarely exceed 40 mm (Li, 2014; Li and Bristow, 2015). The Río Colorado is ephemeral, and although no formal flow gauging records exist, previous observations indicate that small to moderate (sub-bankfull) river flow events occur one or more times in most years, with larger events (bankfull or above) also occurring in most years (Li et al., 2014a, 2019, 2020).

3. Materials and Methods

The GEE platform provides access to Landsat satellite imagery over the last ~40-50 years but in this study we use the GEE platform to generate annual composite images from the Landsat images acquired within the rainy seasons from 2004 through 2016 (Fig. 3 and SI Fig. 1), a time period for which higher resolution (<0.65 m) images are also available. GEE is accessed and controlled through an internet-accessible application programming interface (API) and an associated web-based interactive development environment (IDE) (Gorelick et al., 2017). Therefore, all the methods of data processing outlined in the following sections were performed through coding.

3.1 Materials

We used Landsat 5 and Landsat 8 imagery acquired during the time period of interest (SI Fig. 1; SI Table 1). This imagery is available for all years from 2004 through 2016, except for 2012 and 2013. In the study area, no archived Landsat TM images are available from 2012 onwards and no Landsat 8 data exist for the rainy season of 2012-2013 (SI Fig. 1). Daily precipitation data were collected for the period 2004 through early 2017 from the Bolivian Servicio Nacional de Meteorología e Hidrología in the Uyuni area (SI Fig. 1). For shorter reaches within the study area, higher resolution imagery (<0.65 m) was acquired from Google Earth Pro™ (SI Table 2).

3.2 Methods

3.2.1 Mapping of flooding extent and patterns

To extract flooding extents and patterns, the Landsat images acquired in each rainy season (December through March) were integrated and processed on the GEE platform (SI Fig. 2). Landsat surface reflectance data including Thematic Mapper (TM) and Operational Land Imager (OLI) imagery were preprocessed by subsetting into the region of interest (i.e. mainly along the Río Colorado – Fig. 1c). Images with cloud cover of <10% were then selected (SI Table 1) and processed for cloud masking to remove cloud-covered or cloud-shadowed regions. Within the GEE platform, all the Landsat images that met these requirements were compiled in annual collections. As an example, for the 2016 rainy season, four images (acquired on December 30, January 15, February 16, and March 3) are available and contained in the annual collection (SI Fig. 3). Modified Normalized Difference Water Index (MNDWI) is widely used to extract wet land (‘water bodies’) due to stronger absorption by water of solar radiation in shortwave infrared (SWIR) bands than in near infrared (NIR) and visible bands (Xu, 2006):

$$MNDWI = \frac{\rho_{green} - \rho_{SWIR}}{\rho_{green} + \rho_{SWIR}} \quad (1)$$

where for Landsat TM data, ρgreen is reflectance in Band 2 and ρSWIR is reflectance in Band 5, and for Landsat 8 data, ρgreen is reflectance in Band 3 and ρSWIR is reflectance in Band 6. MNDWI mapping results in an image with values between 1 and -1, whereby pixels with high inundation probability have a high (positive) MNDWI. To map the maximum flooding extent, we made wettest-pixel composites from images in the annual collections. The pixel is considered 'inundation active' when wet land appears in any one image. As such, the annual time-series composite images are generated based on the pixel that contains the maximum MNDWI value from the annual collection (SI Fig. 3).

The imaging of water indices shows a polarisation trend whereby the pixel values of wet land return positively large values, whereas those of other objects tend to be theoretically negative. Thus, the image histogram is characterised by a smoothed, two-peaked representation of the distribution of foreground and background pixels. Histogram shape-based Otsu's method has proven useful for defining the optimal segmentation threshold in the water index image (Yang and Chen, 2017; Yang et al., 2017, 2018, 2020a, 2020b; Li et al., 2018). Thus, the time-series composite images with the wettest pixels were employed to generate the flooding maps (SI Fig. 4) using Otsu's method (Otsu, 1979). Otsu's method was used to determine dynamic thresholds of classification while visual interpretation of flooded areas along with 50 random referenced points (Fig. 1c) was used to examine the classification accuracy. Single pixels were classified as flooded areas if the MNDWI was greater than its threshold value in the time-series composite image. Confusion matrices were used to assess the methods in this study. Using a confusion matrix, pixels in the study area were divided into four classes including TP (true positive), FN (false negative), FP (false positive), and TN (true negative). These four classes represent accurate pixel extraction (TP), missing water bodies (FN), inaccurate extraction (FP), and the accurate rejection (TN) of non-water, respectively. Subsequently, four normalized metrics including producer's accuracy (PA), user's accuracy (UA), overall accuracy, and kappa coefficient were used to assess the performance of the methods. PA indicates completeness, meaning that a low PA indicates high omission error. UA shows correctness, meaning that a low UA indicates an extreme commission error. Following these analyses, flooded land ('wet land'/'water bodies') was mapped and exported as polygons, and areas were calculated using ArcGIS.

3.2.2 Analysis of precipitation data

Daily precipitation data in the study area were processed and extracted to derive 2-day precipitation and 3-day precipitation datasets. From these datasets, yearly daily maximum precipitation, 2-day maximum precipitation and 3-day maximum precipitation were obtained. Rate of change was calculated as the difference between two temporally adjacent values of maximum precipitation, divided by the length of time between the two observation points. These datasets then provided the basis for investigation of the relationships with flooding extent and pattern.

3.2.3 Investigation of channel-floodplain morphodynamics

The high resolution (<0.65 m) satellite imagery (SI Table 2) was used to document and quantify the impact of flooding on channel bank erosion and channel-floodplain morphology. Only imagery for 2004 and 2018 covers the whole study reach but six scenes (2004, 2007, 2010, 2013, 2016 and 2018) cover part of the downstream reaches (see boxed area labelled 'downstream reaches' in Fig. 3a). A total of 52 bends along the trunk channel (reaches C-B, n = 33) and a secondary channel (D1, n = 19) were analysed for various parameters including channel sinuosity (defined as channel distance/straight-line distance), lateral migration rates, and erosional and depositional areas (Fig. 3a). The small number of bends (n = 4) along the shorter channel D2 were not analysed. For analysis, newer high-resolution images were registered to the reference image of 2004 using the remote sensing image analysis software ENVI 5.3. Following standard procedure, the migration distances for single bends between two observation dates were measured at the outer bank. The lateral migration rates were then calculated as the ratio of the migration distance to the length of time between the observation dates. Areas of active erosion and deposition were mapped and exported as polygons, and areas were calculated using ArcGIS. Across all the active, abandoning and abandoned channels, select reaches were also investigated for other evidence of channel-floodplain morphological dynamics (e.g. Fig. 3b-c).

4. Results

4.1 Accuracy assessment

An accuracy threshold plays an important role in differentiating flooded areas (i.e. wet land/water bodies) from dry land areas. During the time period of interest, the average threshold value by Otsu's method is -0.22 (maximum of -0.135, minimum of -0.254) (SI Fig. 5). Between 2004 and 2007, the values fluctuate from -0.212 to -0.135 but between 2008 and 2016 threshold values are more stable at ~-0.25.

For the time period 2004 through 2016, the mean producer's accuracy is 91.68% (minimum of 79.31%), the mean user's accuracy is 97.33% (minimum of 92.86%) and the mean overall accuracy is 93.09% (minimum of 86.00%) (Table 2). The mean kappa coefficient is 0.84 (Table 2). Although the active trunk channel (width <30 m) can be extracted, the main errors in separation of flooded areas and dry land areas occurred in the water-land transition zone near river channel banks. Overall, the results suggest that the Landsat composite-derived MNDWI can be used for detecting flooded areas in the study with a high level of accuracy.

4.2 Flooding extent and pattern in relation to channel-floodplain topography

Mapping shows that during the time period of interest, flooding area averaged 35.8 km^2 (Figs 4 and 5a). Maximum flooding extent occurred in 2006 (up to 48 km^2) while minimum flooding extent occurred in 2011 (14 km^2) (Figs 4 and 5a). In many years, flooding is especially prominent to the west of the trunk channel (active reaches C-B and in the area of abandoned channel A) and around the downstream reaches of the secondary channels D1 and D2 (Fig. 4). Although some flooding might result from direct precipitation and consequent ponding on the floodplain, overbank flow emanating from the trunk and secondary channels clearly also makes a contribution. Along the trunk channel (reach C), the linear nature (narrow, elongated pattern) of some flooded areas demonstrates that at least some floodwater flows through meander cutoffs and remnant depressions created by older, largely abandoned channels on the western side of the floodplain (see Fig. 1c) before returning to the trunk channel (reach B) farther downstream (for the clearest examples, see years 2007 and 2009 in Fig. 4).

4.3 Flooding and precipitation

As expected, across the time period of interest, flooding area shows a strong positive correlation with the different precipitation datasets (Fig. 5a). The correlation between rate of change in flooded area and in 2-day maximum precipitation is slightly stronger (R2 ~ 0.83) than for daily maximum precipitation (R2 ~ 0.74) and 3-day maximum precipitation (R2 ~ 0.77) (Fig. 5b). Although the time period of interest is relatively short (2004 through 2016), and so caution needs to be exercised, the changes in maximum precipitation appear to be broadly in agreement with ENSO dynamics, as reflected in the Multivariate ENSO Index (MEI)(Fig. 5c). Low to negative MEI values indicate La Niña periods and tend to be associated with high maximum precipitation totals and flooded areas (e.g. 2006, 2008), while higher MEI values indicate El Niño periods and tend to be associated with lower maximum precipitation totals and flooded areas (e.g. 2009, 2015) (Fig. 5c). Clearly, however, longer term datasets will be needed to undertake more robust statistical analyses to establish the degree of correspondence between ENSO, rainfall and flooding.

4.4 Channel-floodplain morphodynamics

Analysis of 52 meander bends along the trunk channel (reaches C-B) and secondary channel D1 (Fig. 3a) reveals that many bends are laterally migrating (e.g. Fig. 3b-c) at rates ranging up to 8 m/yr. Lateral migration involves both erosion and deposition (Fig. 3b-c); from an aerial (plan view) perspective, erosion is occurring over an area of 2.245 x 10^5 m^2 (0.2245 km^2) and deposition over an area of 1.518 x 10^5 m^2 (0.1548 km^2). The majority of bends are experiencing more erosion than deposition (SI Fig. 6a and c). Along both reaches C-B and D1, the majority of bends have increased in sinuosity between 2004 and 2018 (SI Fig. 6b and d), leading to increased sinuosity along the channels as a whole.

Channel D1 is currently undergoing gradual abandonment, with flow increasingly shifting to the trunk channel (reach B) in the middle of the study reach (Fig. 1c) as well as to secondary channel D2 farther downvalley (Fig. 1d). The ongoing impacts of this unfolding avulsion are captured by the higher resolution images (Fig. 6). Channel D2 was already present in 2004 but in subsequent years (2007, 2010) widened significantly, and by 2013 was clearly the dominant channel (Fig. 6a-d). Over the same time period, D1 decreased in width (Fig. 6a-d). Flow shifting has been accompanied by significant channel-floodplain topographic development, including levee breaching and crevasse splay formation and extension (Fig. 6b-c). Particularly dense networks of crevasse splays have developed around the channel D1 bend downstream of the avulsion node (Fig. 6b-c), which may be related to sediment infilling along this abandoning bend and associated flow displacement overbank. Farther downstream along channel D2, an additional short reach has also been subject to avulsion (Fig. 1d), with flow increasing shifting from an easterly to a more westerly channel (Fig. 1e). Along this short reach, levee breaching and crevasse splay formation is not yet evident.

5. Interpretation

GEE-based flood visualisation has revealed areas of prominent flooding in the study area, including adjacent to the trunk channel (reaches C-B) and the more downstream reaches of secondary channels D1 and D2 (Fig. 4). At the scale of the study reach, this flooding pattern demonstrates the high degree of channel-floodplain connectivity and further illustrates how complex spatial patterns of water flow on floodplains pose a challenge for hydraulic modelling approaches (c.f. Bridge, 2003). Annual flooding correlated most strongly (R^2 = 0.83) with 2-day maximum precipitation totals (Fig. 5b). This illustrates the importance of considering consecutive days' precipitation when analysing flooding patterns, and provides a counterbalance to the previous emphases on the influence of short-duration (<1 day) precipitation events on flooding and channel-floodplain dynamics along small, arid-zone, ephemeral rivers (e.g. Schick, 1988; Dick et al., 1997; Reid and Frostick, 2011). Although caution needs to be exercised, the tendency for higher precipitation totals and flooding extent to be associated with a low or negative MEI (Fig. 5c) supports allied research in the study area that has revealed how short-term (yearly to decadal) clusters of chute cutoffs on meander bends are closely related to La Niña-driven flood events (Li et al., 2020).

Along with chute cutoff formation (Li et al., 2020), significant bend migration, levee breaching, crevasse splay development, and avulsion has occurred in the study reach during the last couple of decades (Figs

1d-e, 3, 6). The satellite images of the study reach show numerous older, sinuous channels to the west of the current trunk channel (Fig. 1c), suggesting that these avulsion dynamics have been a natural part of longer term (likely centennial to millennial) river system responses. The high degree of channel-floodplain connectivity and rapid (decadal-scale) avulsion dynamics that are so characteristic of this river system enable the sites of potential future avulsions to be identified. For instance, in the upstream reach of the trunk channel (reach C), a headward eroding channel has extended between 2004 and 2018 and is now connected with crevasse channels on an outer meander bend (Fig. 3b-c). During high flows, these crevasse channels will convey flow to the headward eroding channel, likely leading to channel incision and widening, and increasing flow diversion to this newly eroded channel. In turn, this may lead to gradual abandonment of the trunk channel in the reach immediately downstream.

Significantly, however, the evidence from channel D1 shows that flow diversion does not necessarily lead to cessation of meander bend migration in reaches immediately downstream, at least not in the early stages of channel abandonment. Two main avulsion nodes are present along channel D1, with flow diversion to the trunk channel (reach B) taking place in the middle of the study area (Fig. 1c) and flow diversion to secondary channel D2 taking place farther downstream (Fig. 1d). Increasing flow diversion from channel D1 to trunk channel reach B and to D2 has occurred post-2004 (Fig. 6) but many individual bends along D1 nonetheless still experienced significant erosion and became increasingly sinuous between 2004 and 2018 (SI Fig. 6c-d). These findings demonstrate that in this unvegetated, ephemeral river, which is characterised by shallow channels that experience frequent within-channel and overbank flooding, dynamic adjustment of bends can continue to take place even in the early stages of channel abandonment.

Along the active and abandoning channels of the Río Colorado, the ongoing bend adjustments and other channel-floodplain dynamics (e.g. levee breaching and crevasse splay development) are associated with significant erosion (SI Fig. 6a and c). As a consequence, and despite some counterbalancing deposition in point bars, on levees and in splay channels, sediment is exported from the study area to the reaches farther downstream towards the river terminus. In these fan-shaped lower reaches, deposition is more widespread, with progradation of channel-belt sediments occurring across older (pre-late Holocene) lacustrine sediments that are related to a formerly more extensive Salar de Uyuni (Donselaar et al., 2013; Li and Bristow, 2015; Li et al., 2019).

6. Discussion

This study has used a combination of GEE-based flood visualization, secondary datasets, and higher resolution satellite imagery, complementing other recent research that has used various remote sensing approaches to investigate river forms, processes and responses (for overviews, see Carbonneau and Piégay, 2012; Gilvear and Bryant, 2016; Gilvear et al., 2016; Entwistle et al., 2018; Tomsett and Leyland, 2019; Piégay et al., 2020). Similar approaches to those used in our study could be applied to many other rivers globally, but given the difficulties of field observations of flooding and flood impacts in remote drylands, the application to a wider range of dryland rivers may be particularly useful, as discussed in the sections below.

6.1 Wider application of the study approaches

Many previous studies of flood extent, pattern and impact in dryland rivers have relied on single satellite images, despite concerns over high cloud coverage and the known limitations of acquiring images after peak flow has taken place (e.g. Chignell et al., 2015; Li et al., 2018). The generation of Landsat-derived composites using the GEE platform, however, enables analysis of multi-day imagery for a given rainy season, thereby ensuring that all satellite imagery with suitably low cloud cover can be used to increase the accuracy of flood mapping. More accurate mapping is particularly important for those dryland rivers that are characterized by downstream reductions in cross-sectional area, for prominent overbank flooding and marked channel-floodplain dynamics may occur even during moderate floods. Besides the lower Río Colorado (Li et al., 2014a, 2019; Li and Bristow, 2015), examples include various rivers in the Australian and South African drylands (Tooth, 1999, 2000; Tooth et al., 2002, 2014; Ralph and Hesse, 2010; Larkin et al., 2017a, 2020a). Our study approaches could also be applied to other non- or poorly-vegetated, ephemeral rivers such as characterise parts of the southwest USA (Ielpi, 2018; Ielpi and Lapôtre, 2019), or to those dryland rivers where riparian vegetation density and/or health is declining owing to climate change or direct human interventions that have resulted in desiccation, salinisation, pollution, increased fire frequency, or disease (e.g. Stromsoe and Callow, 2012; Jaeger et al., 2017).

6.2 Comparing channel-floodplain dynamics in unvegetated and vegetated dryland rivers

While a substantial body of previous research has focused on flood-related, channel-floodplain dynamics in perennial humid or tropical region rivers (e.g. Parker, 2000; Terry et al., 2002; Schanze et al., 2006; Woodward et al., 2010; Wohl et al., 2012), some research attention has also been directed towards studies of flood impacts in intermittent or ephemeral, dryland rivers (for a summary, see Tooth, 2013). In particular, the dynamics of sparsely-vegetated or non-vegetated, ephemeral dryland rivers have been subject to increasing analysis (e.g. Billi et al., 2018; Ielpi, 2018; Ielpi et al., 2018; Ielpi and Lapôtre, 2019) in part because of increasing recognition that some ephemeral dryland rivers may be highly sensitive systems, whereby sensitivity is defined either in terms of the high propensity for flood-related channel-floodplain dynamics and/or the limited ability to recover from those dynamics (Tooth, 2013; see also Lisenby et al., 2019). Importantly, the high sensitivity of some poorly or non-vegetated, ephemeral dryland rivers can be exploited to provide insight into the longer-term dynamics of more slowly developing dryland rivers. For instance, along with previous studies of the middle and lower Río Colorado and neighbouring Río Capilla, the results of this study show how this system can serve as a large scale natural experiment, with regular La Niña-driven floods driving cascades of channel-floodplain dynamics on (sub-)decadal timescales (cf. Li et al., 2019, 2020), despite low stream powers and cohesive channel perimeter sediments (Table 1). In other disciplines, studies have suggested that the large-scale meteorological shifts associated with ENSO may presage the effects of 21st century regional to global climate change (e.g. Heaney et al., 2019), so these rapid cascades may provide into potential channel-floodplain dynamics in the coming decades. Additionally, the rapid cascades along the Río Colorado provide opportunities to monitor and characterise channel-floodplain dynamics in ways not possible in more vegetated dryland rivers, such as those in Australia and South Africa where otherwise comparable dynamics such as crevasse splay formation, avulsions and headward channel migration have been shown to take place over multidecadal, centennial or longer timescales (e.g. Tooth, 2005; Tooth et al., 2007, 2009, 2014; Larkin et al., 2017b). Along these Australian and South African dryland rivers, unit stream powers during floods tend to be similar to the Río Colorado (<10 W/m^2) and while channel bed sediments may be coarser (sand, minor gravel), channel bank and floodplain sediments also tend to be cohesive (e.g. dominantly clay and silt). This suggests that while the basic patterns and trajectories of the channel-floodplain dynamics may be similar, the slower rates in these other dryland rivers can be attributed to the additional hydraulic roughness and resistance to erosion provided by the riparian vegetation (e.g. grasses and sedges, or grasses and shrubs/trees).

6.3 Implications for dryland river and flood management

Previous studies of dryland rivers have demonstrated how different data-driven, interdisciplinary approaches can play a vital part in improving assessment of channel-floodplain dynamics, with implications for management. In some instances, remote sensing approaches have formed a key component of these study approaches. For instance, Tooth et al. (2014) used a combination of field investigations, geochronology (luminescence dating), and remote sensing (mainly aerial image and orthophotograph interpretations) to reconstruct the historical and longer term (multi-centennial) dynamics of the Blood River floodplain wetlands in dryland South Africa. These reconstructions provided a reference condition against which to assess recent (decadal-scale) channel-floodplain dynamics. Prior to the early part of the last century, the wetlands were characterised by a through-going, meandering channel but over the last 70-80 years, major morphological and sedimentary changes have occurred in the upper part of the wetlands. The former meandering channel has been replaced by a straighter channel that decreases in size downstream and now terminates in a unchannelled reedbed, creating a major discontinuity in downvalley water and sediment transfer that is likely to persist for centuries (Tooth et al., 2014). Along the Blood River, the initial cause(s) of these profound channel-floodplain dynamics are not known but may be related to a period of severely decreased flow in the 1930s and/or anthropogenic impacts (e.g. river damming) (Tooth et al., 2014).

Even in study settings where geochronological constraints on longer term channel-floodplain dynamics are absent and/or remote sensing datasets have a more restricted temporal range, remote sensing image analysis can still help to characterise past river responses and so provide context for assessment of the significance of channel-floodplain dynamics on more recent timescales (e.g. decades). For instance, along the study reach of the Río Colorado, satellite imagery reveals numerous older, sinuous channels to the west of the current trunk channel (Fig. 1c). This evidence suggests that the avulsion dynamics that have characterised parts of the study reach over the last few decades (see also Li et al., 2020) are a natural part of longer term (likely centennial to millennial) river system responses, and are not the result of recent climate change or other human activities in the catchment. In other words, and in stark contrast to the Blood River example where an historically unprecedented channel-floodplain transformation has occurred, the recent dynamics along the Río Colorado are simply part of the expected (i.e. normal) range of longer term, river responses.

The contrast between the recent dynamics of the Blood River and Río Colorado is worth stressing as it illustrates an important point with potential significance for dryland river and flood management. Brierley and Fryirs (2005) make a clear distinction between river behaviour (adjustments to channel-floodplain morphology that help to maintain a characteristic morphology and set of process attributes) and river change (a fundamental shift in morphology and process associations that indicate reach evolution to a different river type). River behaviour (e.g. Río Colorado) and river change (e.g. Blood River) thus may pose different management challenges that require different strategies to cope with the attendant alterations to flood extent and flood patterns. In cases of river behaviour, one management strategy may simply be to accommodate the expected range of channel-floodplain adjustments (e.g. through floodplain land use re-zoning), whereas in cases of river change, more proactive management approaches may be needed (e.g. using structural interventions). During forthcoming decades, it will be particularly important to identify and characterise thresholds of dryland river change (Tooth, 2018; Larkin et al., 2020a, b), especially in cases where altered flooding extent and patterns will threaten ecosystem service delivery (e.g. McCarthy et al., 2010), facilitate the spread of water-associated diseases (e.g. Malan et al., 2009; Smith et al., 2013; Heaney et al., 2019), and/or pose a greater hazard for land use, infrastructure, property and life (e.g. Ashley and Ashley, 2008; Woodward et al., 2010). In a time of rapid environmental change, when dryland rivers globally are responding to climate changes and/or other human activities, new data-driven, interdisciplinary approaches will be needed to help determine this distinction between river behaviour and river change, and also to evaluate the appropriate river and flood management strategies.

7. Conclusions

This study has shown how the GEE platform has helped with the visualisation of flooding extent and patterns along an unvegetated, ephemeral river system, and how analysis and quantification of the floods can be combined with other datasets (precipitation, higher resolution imagery) to provide insights into channel-floodplain dynamics on recent, observable timescales. The findings from the Río Colorado improve our understanding of the dynamics of this river in particular, but also provide scope for comparison with the channel-floodplain dynamics of a wider range of dryland rivers in different physiographic contexts, including those with different levels of riparian vegetation.

Of particular value in future research will be additional datasets on short-term (yearly to decadal scale) patterns, rates and timescales of dryland river dynamics, particularly where this improves our ability to distinguish between river behaviour involving channel-floodplain adjustments that remain within the expected range, and river change involving more profound, threshold-based, channel-floodplain changes. Given the strong links between dryland channel-floodplain dynamics, water-associated infectious diseases, and many other aspects of catchment ecosystem service delivery and hazard assessment (Millennium Ecosystem Assessment, 2005), clear potential exists for further data-driven, interdisciplinary studies. In a time of rapid environmental changes, one increasingly defined by humanity's direct and indirect impacts on the Earth system, development of more remote sensing-based approaches should form an essential part of these interdisciplinary studies. This will help to improve visualisation of flooding and associated channel-floodplain dynamics, so providing a key underpinning for dryland river management policy and practice.

Acknowledgements

This research was supported by: the National Natural Science Foundation of China (No. 41972114, No. 41602121); the Wuhan Applied Foundational Frontier Project (No. 2020020601012281); the Fundamental Research Funds for the Central Universities, China University of Geosciences (Wuhan) (No. CUG150616); and Open Fund (TPR-2017-01) of Key Laboratory (Ministry of Education) of Tectonics and Petroleum Resources (China University of Geosciences, Wuhan, China). J.L. thanks colleagues Oswaldo Eduardo Ramos Ramos, Rafael Cortez, and students Edson Wilder Ramos Mendoza, Wilhelm Alex Mendizabal Cuevas, Samir Nikolar Pacheco, Erick Marcelo Cabero Caballero, Julian Franz Cortez Garvizu (all from Universidad Mayor de San Andrés) for the fieldwork arrangements and assistance near Salar de Uyuni in Bolivia. JL thanks German Aerospace Center for the TanDEM-X data (Grant no. GEOL2320).

References

Ashley, S.T., Ashley, W.S. (2008). Flood fatalities in the United States. J. Appl. Meteorol. Climatol., 47, 805–818. https://doi.org/10.1175/2007JAMC1611.1

Baucom, P.C., Rigsby, C. A. (1999). Climate and lake-level history of the northern Altiplano, Bolivia, as recorded in Holocene sediments of the Rio Desaguadero. J. Sediment. Res., 69, 597–611. https://doi.org/10.2110/jsr.69.597

Billi, P., Demissie, B., Nyssen, J., Moges, G., Fazzini, M., (2018). Meander hydromorphology of ephemeral streams: similarities and differences with perennial rivers. Geomorphology 319, 35–46.

Bills, B.G., de Silva, S.L., Currey, D.R., Emenger, R.S., Lillquist, K.D., Donnellan, A., Worden, B. (1994). Hydro-isostatic deflection and tectonic tilting in the central Andes: Initial results of a GPS survey of Lake Minchin shorelines. Geophys. Res. Lett., 21, 293–296. https://doi.org/10.1029/93GL03544

Bridge, J.S. (2003). Rivers and Floodplains: Forms, Processes and the Sedimentary Record, Blackwell, 491 pp.

Brierley, G.J., Fryirs, K.A. (2005). Geomorphology and River Management: Applications of the River Styles Framework. Wiley-Blackwell, 416 pp.

Carbonneau, P.E., Piégay, H. (2012). Fluvial Remote Sensing for River Science and Management. Wiley.

Carroll, R.W.H., Warwick, J.J., James, A.I., Miller, J.R. (2004). Modeling erosion and overbank deposition during extreme flood conditions on the Carson River, Nevada. J. Hydrol. 297, 1–21. https://doi.org/10.1016/j.jhydrol.2004.04.012

Chignell, S.M., Anderson, R.S., Evangelista, P.H., Laituri, M.J., Merritt, D.M. (2015). Multi-temporal independent component analysis and Landsat 8 for delineating maximum extent of the 2013 Colorado Front Range flood. Remote Sens., 7, 9822–9843. https://doi.org/10.3390/rs70809822

Clement, M. A., Kilsby, C. G., Moore, P. (2018). Multi-temporal synthetic aperture radar flood mapping using change detection. Journal of Flood Risk Management, 11(2), 152–168. https://doi.org/10.1111/jfr3.12303

DeVries, B., Huang, C., Armston, J., Huang, W., Jones, J. W., Lang, M. W. (2020). Rapid and robust monitoring of flood events using Sentinel-1 and Landsat data on the Google Earth Engine. Remote Sensing of Environment, 240, 111664. https://doi.org/10.1016/j.rse.2020.111664

Dick, G.S., Anderson, R.S., Sampson, D.E. (1997). Controls on flash flood magnitude and hydrograph shape, Upper Blue Hills badlands, Utah. Geology, 25, 45–48. https://doi.org/10.1130/0091-7613(1997)025<0045:COFFMA>2.3.CO;2

Domeneghetti, A., Schumann, G.J.P., Tarpanelli, A. (2019). Preface: Remote sensing for flood mapping and monitoring of flood dynamics. Remote Sens., 11, 11–14. https://doi.org/10.3390/rs11080940

Donselaar, M.E., Gozalo, M.C.C., Moyano, S. (2013). Avulsion processes at the terminus of low-gradient semi-arid fluvial systems: Lessons from the Río Colorado, Altiplano endorheic basin, Bolivia. Sediment. Geol., 283, 1–14. https://doi.org/10.1016/j.sedgeo.2012.10.007

Entwistle N, Heritage G, Milan D. (2018). Recent remote sensing applications for hydro and morphodynamic monitoring and modelling. Earth Surface Processes and Landforms, 43, 2283–2291.

Foody, G.M., Ghoneim, E.M., Arnell, N.W. (2004). Predicting locations sensitive to flash flooding in an arid environment. J. Hydrol., 292, 48–58. https://doi.org/10.1016/j.jhydrol.2003.12.045

Gilvear, D, Bryant, R. (2016). Analysis of remotely sensed data for fluvial geomorphology and river science. In Kondolf GM, Piégay H (eds), Tools in Fluvial Geomorphology, 2nd edn. Wiley: Chichester, UK; 103–132.

Gilvear, D.J., Hunter, P., Stewardson, M., Greenwood, M.T., Thoms, M.C., Wood, P.J. (2016). Remote sensing: mapping natural and managed river corridors from the micro to the network scale. In Gilvear, D.J., Greenwood, M.T., Thoms, M.C., Wood, P.J. (eds). River Science: Research and Management for the 21st Century, Wiley: Chichester, UK; 171–196.

Gleeson, T. Wang-Erlandsson, L., Porkka, M., Zipper, S.C., Jaramillo, F., Gerten, D., Fetzer, I., Cornell, S.E., Piemontese, L., Gordon, L.J., Rockström, J., Oki, T., Sivapalan, M., Wada, Y., Brauman, K.A., Flörke, M., Bierkens, M.F.P., Lehner, B., Keys, P., Kummu, M., Wagener, T., Dadson, S., Troy, T.J., Steffen, W., Falkenmark, M., Famiglietti, J.S. (2020). Illuminating water cycle modifications and Earth System resilience in the Anthropocene. Water Resources Research, 56, e2019WR024957.

Gorelick, N., Hancher, M., Dixon, M., Ilyushchenko, S., Thau, D., Moore, R. (2017). Google Earth Engine: Planetary-scale geospatial analysis for everyone. Remote Sens. Environ., 202, 18–27. https://doi.org/10.1016/j.rse.2017.06.031

Gumbricht, T., Wolski, P., Frost, P., Mccarthy, T.S. (2004). Forecasting the spatial extent of the annual flood in the Okavango delta, Botswana. J. Hydrol., 290, 178–191.

Heaney, A.K., Shaman, J. and Alexander, K.A. (2019). El Niño-Southern oscillation and under-5 diarrhea in Botswana. Nature Communications, 10, 5798.

Heritage, G., Entwistle, N., Milan, D., Tooth, S. (2019). Quantifying and contextualising cyclone-driven, extreme flood magnitudes in bedrock-influenced dryland rivers. Adv. Water Resour., 123, 145–159. https://doi.org/S0309170818303828

Hoegh-Guldberg, O., Jacob, D., Taylor, M., Bindi, M., Brown, S., Camilloni, I., Diedhiou, A., Djalante, R., Ebi, K.L., Engelbrecht, F., Guiot, J., Hijioka, Y., Mehrotra, S., Payne, A., Seneviratne, S.I., Thomas, A., Warren, R. and Zhou, G. (2018). Impacts of 1.5ºC global warming on natural and human systems. In: Masson-Delmotte, V., Zhai, P., Pörtner, H.-O., Roberts, D., Skea, J., Shukla, P.R., Pirani, A., Moufouma-Okia, W., Péan, C., Pidcock, R., Connors, S., Matthews, J.B.R., Chen, Y., Zhou, X., Gomis, M.I., Lonnoy, E., Maycock, T., Tignor, M. and Waterfield T. (eds.). Global Warming of 1.5°C. An IPCC Special Report on the Impacts of Global Warming of 1.5°C above pre-industrial levels and related global greenhouse gas emission pathways, in the context of strengthening the global response to the threat of climate change, sustainable development, and efforts to eradicate poverty. IPCC.

Hooke, J.M. (2000). Geomorphological impacts of a flood event on ephemeral channels in SE Spain. Geomorphology, 34, 163–180. https://doi.org/10.1016/j.geomorph.2016.03.021

Hooke, J.M. (2016). Geomorphological impacts of an extreme flood in SE Spain. Geomorphology, 263, 19–38. https://doi.org/10.1016/j.geomorph.2016.03.021

Horton, B.K., Decelles, P.G. (2001). Modern and ancient fluvial megafans in the foreland basin system of the central Andes, southern Bolivia: implications for drainage network evolution in fold‐thrust belts. Basin Res., 13, 43–63.

Ielpi, A. (2018). Morphodynamics of meandering streams devoid of plant life: Amargosa River, Death Valley, California. GSA Bull., 131, 782–802. https://doi.org/10.1130/B31960.1

Ielpi A, Fralick P, Ventra D, Ghinassi M, Lebeau L, Marconato A, Meek R, Rainbird RH. (2018). Fluvial floodplains prior to greening of the continents: stratigraphic record, geodynamic setting, and modern analogues. Sedimentary Geology, 372,140–172.

Ielpi, A., Lapôtre, M.G.A. (2019). Barren meandering streams in the Modern Toiyabe Basin of Nevada, U.S.A., and their relevance to the study of the pre-vegetation rock record. J. Sediment. Res., 89, 399–415. https://doi.org/10.2110/jsr.2019.25

Ip, F., Dohm, J.M., Baker, V.R., Doggett, T., Davies, A.G., Castaño, R., Chien, S., Cichy, B., Greeley, R., Sherwood, R., Tran, D., Rabideau, G. (2006). Flood detection and monitoring with the Autonomous Sciencecraft Experiment onboard EO-1. Remote Sens. Environ., 101, 463–481.

IPCC (2014). Climate Change 2014: Synthesis Report. Contribution of Working Groups I, II and III to the Fifth Assessment Report of the Intergovernmental Panel on Climate Change, IPCC.

Jaeger, K.L., Sutfin, N.A., Tooth, S., Michaelides, K., Singer, M. (2017). Geomorphology and sediment regimes of intermittent rivers and ephemeral streams. In: Datry, T., Bonada, N. and Boulton, A. (eds), Intermittent Rivers and Ephemeral Streams: Ecology and Management. London: Academic Press, Elsevier, pp.21-49.

Larkin, Z.T., Tooth, S., Ralph, T.J., Duller, G.A.T., McCarthy, T., Keen-Zebert, A., Humphries, M.S. (2017a). Timescales, mechanisms, and controls of incisional avulsions in floodplain wetlands: Insights from the Tshwane River, semiarid South Africa. Geomorphology, 283, 158–172. https://doi.org/10.1016/j.geomorph.2017.01.021

Larkin, Z.T., Ralph, T.J., Tooth, S., McCarthy, T.S. (2017b). The interplay between extrinsic and intrinsic controls in determining floodplain wetland characteristics in the South African drylands. Earth Surf. Process. Landforms, 42, 1092–1109.

Larkin, Z.T., Ralph, T.J., Tooth, S., Duller, G.A.T. (2020a). A shifting 'river of sand': the profound response of Australia's Warrego River to Holocene hydroclimatic change. Geomorphology, 370, 107385.

Larkin, Z.T., Ralph, T.J., Tooth, S., Fryirs, K.A., Carthey, A.J.R. (2020b). Identifying threshold responses of Australian dryland rivers to future global hydroclimatic change. Scientific Reports, 10, article no. 6653.

Lenters, J.D., Cook, K.H. (1999). Summertime precipitation variability over South America: Role of the large-scale circulation. Mon. Weather Rev., 127, 409–431.

Li, J. (2014). Terminal fluvial systems in a semi-arid endorheic basin, Salar de Uyuni (Bolivia). Uitgeverij BOX Press, 's-Hertogenbosch, The Netherlands.

Li, J., Bristow, C.S. (2015). Crevasse splay morphodynamics in a dryland river terminus: Río Colorado in Salar de Uyuni Bolivia. Quat. Int., 377, 71–82. https://doi.org/10.1016/j.quaint.2014.11.066

Li, J., Donselaar, M.E., Hosseini Aria, S.E., Koenders, R., Oyen, A.M. (2014a). Landsat imagery-based visualization of the geomorphological development at the terminus of a dryland river system. Quat. Int., 352, 100–110. https://doi.org/10.1016/j.quaint.2014.06.041

Li, J., Menenti, M., Mousivand, A., Luthi, S.M. (2014b). Non-vegetated playa morphodynamics using multi-temporal landsat imagery in a semi-arid endorheic basin: Salar de Uyuni, Bolivia. Remote Sens., 6, 10131–10151. https://doi.org/10.3390/rs61010131

Li, J., Bristow, C.S., Luthi, S.M., Donselaar, M.E. (2015a). Dryland anabranching river morphodynamics: Río Capilla, Salar de Uyuni, Bolivia. Geomorphology, 250, 282–297. https://doi.org/10.1016/j.geomorph.2015.09.011

Li, J., Luthi, S.M., Donselaar, M.E., Weltje, G.J., Prins, M.A., Bloemsma, M.R. (2015b). An ephemeral meandering river system: Sediment dispersal processes in the Río Colorado, Southern Altiplano Plateau, Bolivia. Zeitschrift für Geomorphol., 59, 301–317. https://doi.org/10.1127/zfg/2014/0155

Li, J., Yang, X., Maffei, C., Tooth, S., Yao, G. (2018). Applying independent component analysis on Sentinel-2 imagery to characterize geomorphological responses to an extreme flood event near the non-vegetated Río Colorado Terminus, Salar de Uyuni, Bolivia. Remote Sens., 10, 725.

Li, J., Tooth, S., Yao, G. (2019). Cascades of sub-decadal, channel-floodplain changes in low-gradient, non-vegetated reaches near a dryland river terminus: Salar de Uyuni, Bolivia. Earth Surf. Process. Landforms, 44, 490–506. https://doi.org/10.1002/esp.4512

Li, J., Grenfell, M.C., Wei, H., Tooth, S., Ngiem, S. (2020). Chute cutoff-driven abandonment and sedimentation of meander bends along a fine-grained, non-vegetated, ephemeral river on the Bolivian Altiplano. Geomorphology, 350, 106917. https://doi.org/10.1016/j.geomorph.2019.106917

Li, J., Zhao, Y., Bates, P., Neal, J., Tooth, S., Hawker, L., Maffei, C., Duan, S. (2021), Digital Elevation Models for topographic characterisation and flood flow modelling along low-gradient, terminal dryland rivers: a comparison of spaceborne datasets for the Río Colorado, Bolivia, Journal of Hydrology, in

press.
Lisenby, P.E., Tooth, S., Ralph, T.J. (2019). Product vs. process? The role of geomorphology in wetland characterization. Sci. Total Environ., 663, 980–991. https://doi.org/10.1016/j.scitotenv.2019.01.399
Malan, H.L., Appleton, C.C., Day, J.A., Dini, J. (2009). Wetlands and invertebrate disease hosts: are we asking for trouble? Water SA, 35, 753-767.
Marshall, L.G., Swisher III, C.C., Lavenu, A., Hoffstetter, R., Curtis, G.H. (1992). Geochronology of the mammal-bearing late Cenozoic on the northern Altiplano, Bolivia. J. South Am. Earth Sci., 5, 1–19.
McCarthy, T.S., Tooth, S., Kotze, D.C., Collins, N., Wandrag, G., Pike, T. (2010). The role of geomorphology in evaluating remediation options for floodplain wetlands: the case of Ramsar-listed Seekoeivlei, eastern South Africa. Wetlands Ecology and Management, 18, 119-134.
Milan, D., Heritage, G., Tooth, S., Entwistle, N. (2018). Morphodynamics of bedrock-influenced dryland rivers during extreme floods: Insights from the Kruger National Park, South Africa. GSA Bull., 1–17. https://doi.org/10.1130/B31839.1
Millennium Ecosystem Assessment (2005). Ecosystems and Human Well-Being: Wetlands and Water. Synthesis. World Resour. Institute, Washington, DC. https://doi.org/10.1080/17518253.2011.584217
Milzow, C., Kgotlhang, L., Kinzelbach, W., Meier, P., Bauer-Gottwein, P. (2009). The role of remote sensing in hydrological modelling of the Okavango Delta, Botswana. J. Environ. Manage., 90, 2252–2260. https://doi.org/10.1016/j.jenvman.2007.06.032
Nicholas, A.P., Walling, D.E. (1997). Modelling flood hydraulics and overbank deposition on river floodplain. Earth Surf. Process. Landforms, 22, 59–77.
Otsu, N. (1979). A threshold selection method from gray-level histograms. IEEE Trans. Syst. Man. Cybern., 9, 62–66. https://doi.org/10.1109/TSMC.1979.4310076
Parker, D. (2000). Floods (2 Volumes). Routledge, London.

Pekel, J.F., Cottam, A., Gorelick, N., Belward, A.S. (2016). High-resolution mapping of global surface water and its long-term changes. Nature, 540, 418–422. https://doi.org/10.1038/nature20584

Piégay, H., Arnaud, F., Belletti, B., Bertrand, M., Bizzi, S., Carbonneau, P., Dufour, S., Liebault, F., Ruiz-Villanueva, V., Slater, L. (2020). Remotely sensed rivers in the Anthropocene: state of the art and prospects. Earth Surface Processes and Landforms, 45, 157-188.

Ralph, T.J., Hesse, P.P. (2010). Downstream hydrogeomorphic changes along the Macquarie River, southeastern Australia, leading to channel breakdown and floodplain wetlands. Geomorphology, 118, 48–64. https://doi.org/10.1016/j.geomorph.2009.12.007

Reid I., Frostick L.E. (2011). Channel form, flows and sediments in deserts. In: Thomas, D.S.G. (ed.), Arid Zone Geomorphology: Process, Form and Change in Drylands. John Wiley & Sons, Ltd., Chichester, pp. 301–332.

Rigsby, C.A., Bradbury, J.P., Baker, P.A., Rollins, S.M., Warren, M.R. (2005). Late Quaternary palaeolakes, rivers, and wetlands on the Bolivian Altiplano and their palaeoclimatic implications. J. Quat. Sci., 20, 671–691. https://doi.org/10.1002/jqs.986

Rowberry, M.D., McCarthy, T.S., Thompson, M., Nomnganga, A., Moyo, L. (2011). The spatial and temporal characterisation of flooding within the floodplain wetland of the Nyl River, Limpopo Province, South Africa. Water SA, 37, 445-451.

Schanze, J., Zeman, E., Marsalek, J. (2006). Flood Risk Management: Hazards, Vulnerability and Mitigation Measures. NATO Science Series, IV Earth and Environmental Sciences, 67. Springer, The Netherlands.

Schick, A.P. (1988). Hydrologic aspects of floods in extreme arid environments. In: Baker, R., Kochel, R.C., Patton, P.C. (eds.), Flood Geomorphology. Wiley, New York, pp. 189–203.

Slingerland, R., Smith, N.D. (2004). River avulsion and their deposits. Annu. Rev. Earth Planet. Sci., 32, 257–285.

Smith, M.W., Macklin M.G., Thomas, C.J. (2013). Hydrological and geomorphological controls of malaria transmission. Earth-Science Reviews, 116, 109-127.

Stromsoe, N., Callow, J.N. (2012). The role of vegetation in mitigating the effects of landscape clearing upon dryland stream response trajectory and restoration potential. Earth Surf. Process. Landforms, 37, 180–192. https://doi.org/10.1002/esp.2240

Terry, J.P., Garimella, S., Kostaschuk, R.A. (2002). Rates of floodplain accretion in a tropical island river system impacted by cyclones and large floods. Geomorphology, 42, 171–182. https://doi.org/10.1016/S0169-555X(01)00084-8

Thito, K., Wolski, P., Murray-Hudson, M. (2016). Mapping inundation extent, frequency and duration in the Okavango Delta from 2001 to 2012. African J. Aquat. Sci., 41, 267–277. https://doi.org/10.2989/16085914.2016.1173009

Ticehurst, C., Guerschman, J.P., Chen, Y. (2014). The strengths and limitations in using the daily MODIS open water likelihood algorithm for identifying flood events. Remote Sens., 6, 11791–11809. https://doi.org/10.3390/rs61211791

Tomsett C, Leyland J. (2019). Remote sensing of river corridors: a review of current trends and future directions. River Research and Applications, 35, 779–803.

Tooth, S. (1999). Floodouts in central Australia, in: Miller, A.J. and Gupta, A. (ed.), Varieties of Fluvial Form. John Wiley and Sons, Chichester, pp. 219–247.

Tooth, S. (2000). Downstream changes in dryland river channels: the Northern Plains of arid central Australia. Geomorphology, 34, 33–54. https://doi.org/10.1016/S0169-555X(99)00130-0

Tooth, S. (2005). Splay formation along the lower reaches of ephemeral rivers on the Northern Plains of arid central Australia. J. Sediment. Res., 75, 636–649. https://doi.org/10.2110/jsr.2005.052

Tooth, S. (2013). Dryland fluvial environments: assessing distinctiveness and diversity from a global perspective. In: Shroder, J. (Editor in Chief) and Wohl, E.E. (ed.), Treatise on Geomorphology. Academic Press, San Diego, CA, Vol. 9, Fluvial Geomorphology, pp. 612-644 (DOI: 10.1016/B978-0-12-374739-6.00257-8).

Tooth, S. (2018). The geomorphology of wetlands in drylands: Resilience, nonresilience, or …? Geomorphology, 305, 33–48. https://doi.org/10.1016/j.geomorph.2017.10.017

Tooth, S., McCarthy, T.S., Brandt, D., Hancox, P.J., Morris, R. (2002). Geological controls on the formation of alluvial meanders and floodplain wetlands: The example of the Klip River, eastern Free State, South Africa. Earth Surf. Process. Landforms, 27, 797–815. https://doi.org/10.1002/esp.353

Tooth, S., McCarthy, T., Rodnight, H., Keen-Zebert, A., Rowberry, M., Brandt, D. (2014). Late Holocene development of a major fluvial discontinuity in floodplain wetlands of the Blood River, eastern South Africa. Geomorphology, 205, 128–141.

Tooth, S., Rodnight, H., Duller, G.A.T., McCarthy, T.S., Marren, P.M., Brandt, D. (2007). Chronology and controls of avulsion along a mixed bedrock-alluvial river. Bull. Geol. Soc. Am., 119, 452–461. https://doi.org/10.1130/B26032.1

Tooth, S., Rodnight, H., McCarthy, T.S., Duller, G.A.T., Grundling, A.T. (2009). Late Quaternary dynamics of a South African floodplain wetland and the implications for assessing recent human impacts. Geomorphology, 106, 278–291. https://doi.org/10.1016/j.geomorph.2008.11.009

Uddin, K., Matin, M. A., Meyer, F. J. (2019). Operational flood mapping using multi-temporal Sentinel-1 SAR images: A case study from Bangladesh. Remote Sensing, 11(13), 1581. https://doi.org/10.3390/rs11131581

van Toorenenburg, K.A., Donselaar, M.E., Weltje, G.J. (2018). The life cycle of crevasse splays as a key mechanism in the aggradation of alluvial ridges and river avulsion. Earth Surf. Process. Landforms, 43, 2409–2420. https://doi.org/10.1002/esp.4404

Wohl, E., Barros, A., Brunsell, N., Chappell, N.A., Coe, M., Giambelluca, T., Goldsmith, S., Harmon, R., Hendrickx, J.M.H., Juvik, J., McDonnell, J., Ogden, F. (2012). The hydrology of the humid tropics. Nat. Clim. Chang., 2, 655–662. https://doi.org/10.1038/nclimate1556

Woodward, J.C., Tooth, S., Brewer, P.A., Macklin, M.G. (2010). The 4th International Palaeoflood Workshop and trends in palaeoflood science. Glob. Planet. Chang., 70, 1–4. https://doi.org/10.1016/j.gloplacha.2009.11.002

Xu, H. (2006). Modification of normalised difference water index (NDWI) to enhance open water features in remotely sensed imagery. Int. J. Remote Sens., 27, 3025–3033.

Yang, X., Chen, L. (2017). Evaluation of automated urban surface water extraction from Sentinel-2A imagery using different water indices. Journal of Applied Remote Sensing, 11(2), 026016. https://doi.org/10.1117/1.JRS.11.026016

Yang, X., Zhao, S., Qin, X., Zhao, N., Liang, L. (2017). Mapping of urban surface water bodies from sentinel-2 MSI imagery at 10 m resolution via NDWI-based image sharpening. Remote Sensing, 9(6), 1–19.

Yang, X., Qin, Q., Grussenmeyer, P., Koehl, M. (2018). Urban surface water body detection with suppressed built-up noise based on water indices from Sentinel-2 MSI imagery. Remote Sensing of Environment, 219(September), 259–270. https://doi.org/10.1016/j.rse.2018.09.016

Yang, X., Chen, Y., Wang, J. (2020a). Combined use of Sentinel-2 and Landsat 8 to monitor water surface area dynamics using Google Earth Engine. Remote Sensing Letters, 11(7), 687–696. https://doi.org/10.1080/2150704X.2020.1757780

Yang, X., Qin, Q., Yésou, H., Ledauphin, T., Koehl, M., Grussenmeyer, P., Zhu, Z., (2020b). Monthly estimation of the surface water extent in France at a 10-m resolution using Sentinel-2 data. Remote

Sensing of Environment, 244(March), 111803.

List of figures

Fig. 1 The Altiplano and the Río Colorado: (a) location of the Altiplano in South America; (b) map of the Altiplano, highlighting the study reach of the Río Colorado (red box) near the southeastern margin of the Salar de Uyuni; (c) details of the study reach, showing three avulsion nodes (blue dots), random points used for accuracy assessment of flood mapping (red symbols), and the areas covered by some subsequent figures (red boxes); (d) image showing the downstream reach of abandoning channel D1 and newer channel D2; (e) image highlighting an ongoing avulsion along channel D2; (f) TanDEM-X digital elevation model illustrating the characteristically low gradients in the study area.

Fig. 2 Ground level photos showing the typical channel-floodplain characteristics in the study area: (a) point bar and adjacent channel bed on meander bend 33 along reach B (see the locality in Fig. 3, flow direction away from the camera); (b) channel bed, cutbank and adjacent floodplain surface in the upstream limb of meander bend 33 along reach B (see the locality in Fig. 3, flow direction towards the camera). In both (a) and (b), note the absence of vegetation and the fine-grained sediments (clay, silt, fine sand).

Fig. 3 (a) Meander bends analyzed in this study along the trunk channel (reach C-B) and a secondary channel (D1) of the Río Colorado (for location, see Fig. 1c). (b)-(c) Example of channel-floodplain dynamics occurring along a short reach of the trunk channel between November 2004 and November 2018 (for location, see Part a).

Fig. 4 Flood maps for the study reach for the years 2004 through 2016 (nb. no Landsat data is available for the years 2012 and 2013 – see SI Table 1). The red lines indicate the trunk channel (reaches C-B) and the secondary channel D1 (see Fig. 1(c)).

Fig. 5 (a) Flooded area in the study reach for the years 2004 through 2016 in comparison to maximum precipitation totals (daily, 2-day, and 3-day); (b) Relationship between rate of change in flooded area (i.e. 'wet land'/'water bodies') and in maximum precipitation totals (daily, 2-day and 3-day), with rate of change calculated as the difference between two temporally adjacent values, divided by the length of time between the two observation points; (c) Multivariate ENSO Index (MEI) for the years 2004 through 2016; MEI values greater than 0 indicate El Niño years and MEI values lower than 0 indicate La Niña years (data available from https://www.esrl.noaa.gov/psd/enso/mei/table.html).

Fig. 6 Satellite images (a-f) illustrating an avulsion in a downstream part of secondary channel D1 between November 2004 and November 2018 (for location, see Fig. 1c–d and for scale, see Part a). Increasingly, flow has been diverted from D1 to another secondary channel (D2), leading to gradual abandonment of D1, breaching of levees, and formation and extension of crevasse splays.

List of tables

Table 1 Summary of the characteristics of the channels and floodplain that were the main focus of study.

Table 2 Statistics of classification accuracy for Landsat composite images from 2004 through 2016, based on accuracy assessment using visual interpretation and random points.

Fig.1

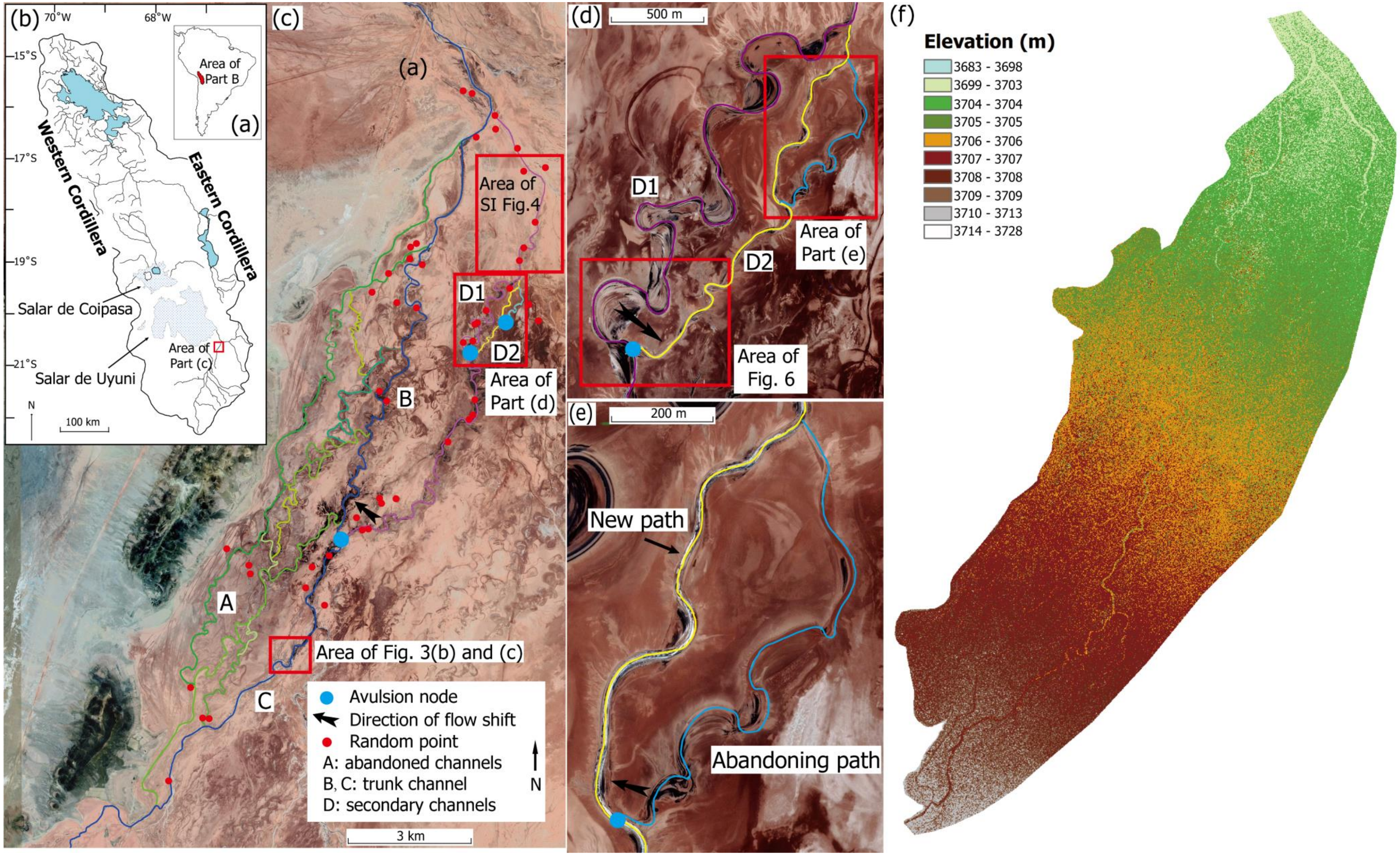

(b)
70°W
68°W
15°S
17°S
19°S
21°S
Western Cordillera
Eastern Cordillera
Salar de Coipasa
Salar de Uyuni
Area of Part (c)
N
100 km
Area of Part B
(a)
(c)
(a)
Area of SI Fig.4
D1
D2
Area of Part (d)
B
A
C
Area of Fig. 3(b) and (c)
Avulsion node
Direction of flow shift
Random point
A: abandoned channels
B, C: trunk channel
D: secondary channels
N
3 km
(d)
500 m
D1
D2
Area of Part (e)
Area of Fig. 6
(e)
200 m
New path
Abandoning path
(f)
Elevation (m)
3683 - 3698
3699 - 3703
3704 - 3704
3705 - 3705
3706 - 3706
3707 - 3707
3708 - 3708
3709 - 3709
3710 - 3713
3714 - 3728

Fig.2

Fig.3

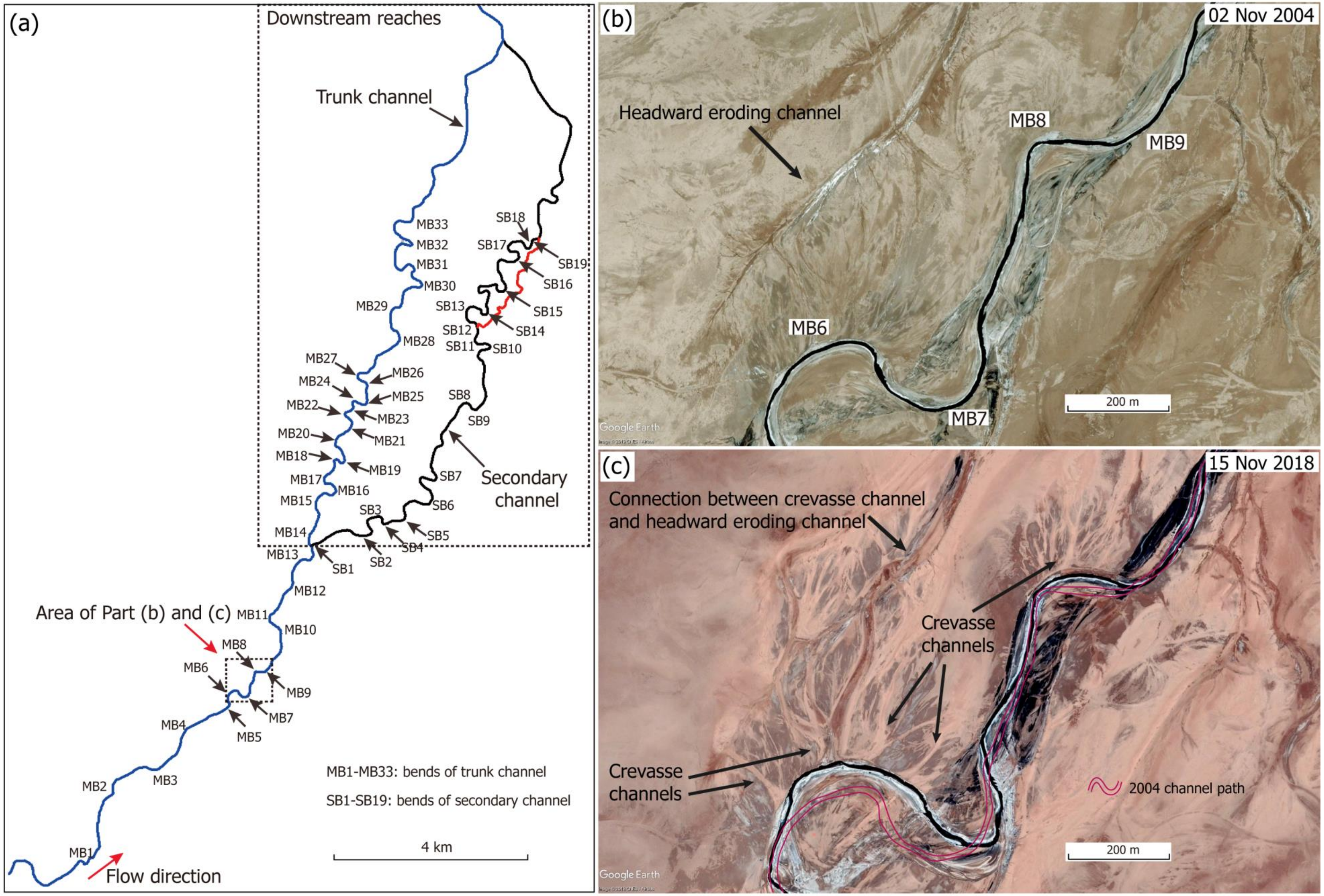
(a)
Downstream reaches
Trunk channel
Secondary channel
Area of Part (b) and (c)
Flow direction
MB1-MB33: bends of trunk channel
SB1-SB19: bends of secondary channel
4 km
(b)
02 Nov 2004
Headward eroding channel
MB6
MB7
MB8
MB9
200 m
(c)
15 Nov 2018
Connection between crevasse channel
and headward eroding channel
Crevasse channels
Crevasse channels
2004 channel path
200 m

Fig.4

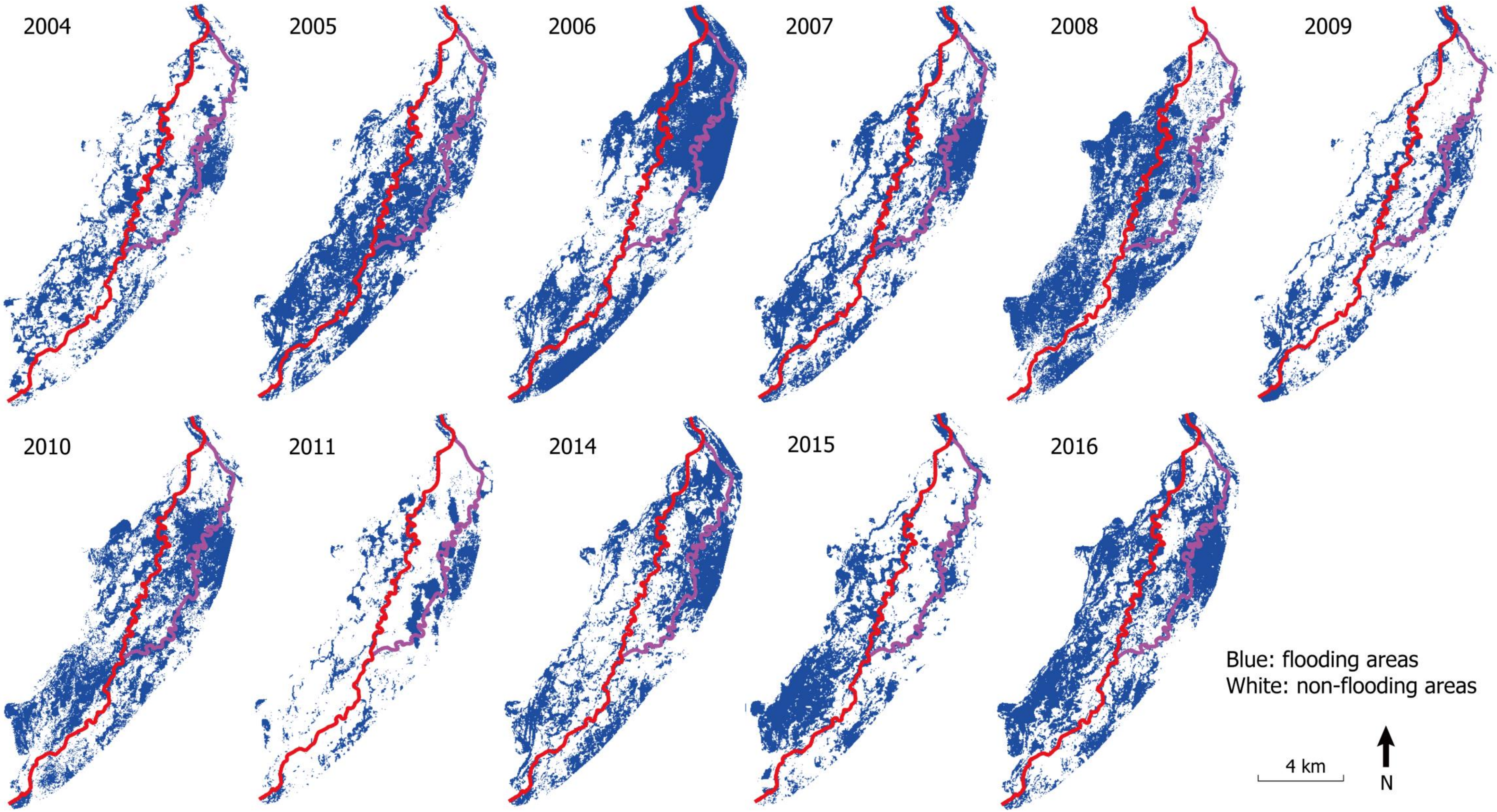
2004
2005
2006
2007
2008
2009
2010
2011
2014
2015
2016
Blue: flooding areas
White: non-flooding areas
4 km
N

Fig.5

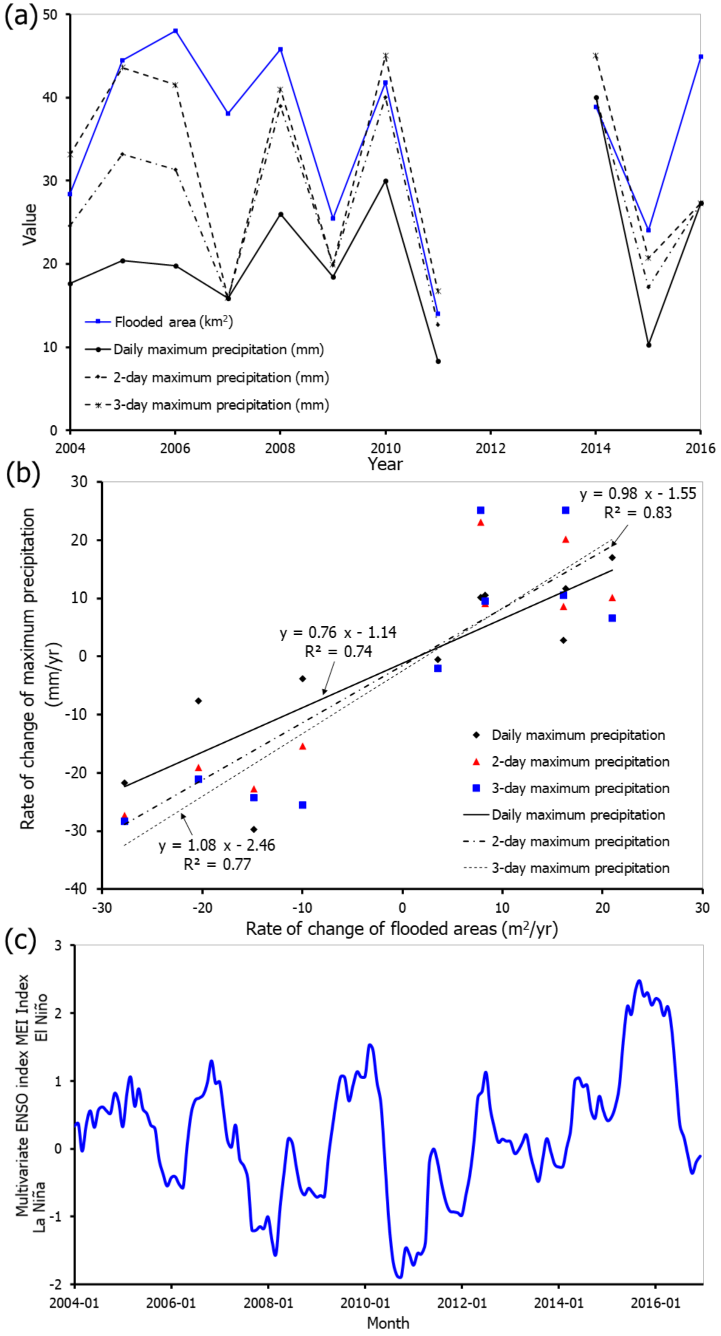
(a)
Value
Year
Flooded area (km2)
Daily maximum precipitation (mm)
2-day maximum precipitation (mm)
3-day maximum precipitation (mm)
(b)
Rate of change of maximum precipitation (mm/yr)
Rate of change of flooded areas (m2/yr)
y = 0.98 x - 1.55
R² = 0.83
y = 0.76 x - 1.14
R² = 0.74
y = 1.08 x - 2.46
R² = 0.77
Daily maximum precipitation
2-day maximum precipitation
3-day maximum precipitation
(c)
Multivariate ENSO index MEI Index
El Niño
La Niña
Month

Fig.6

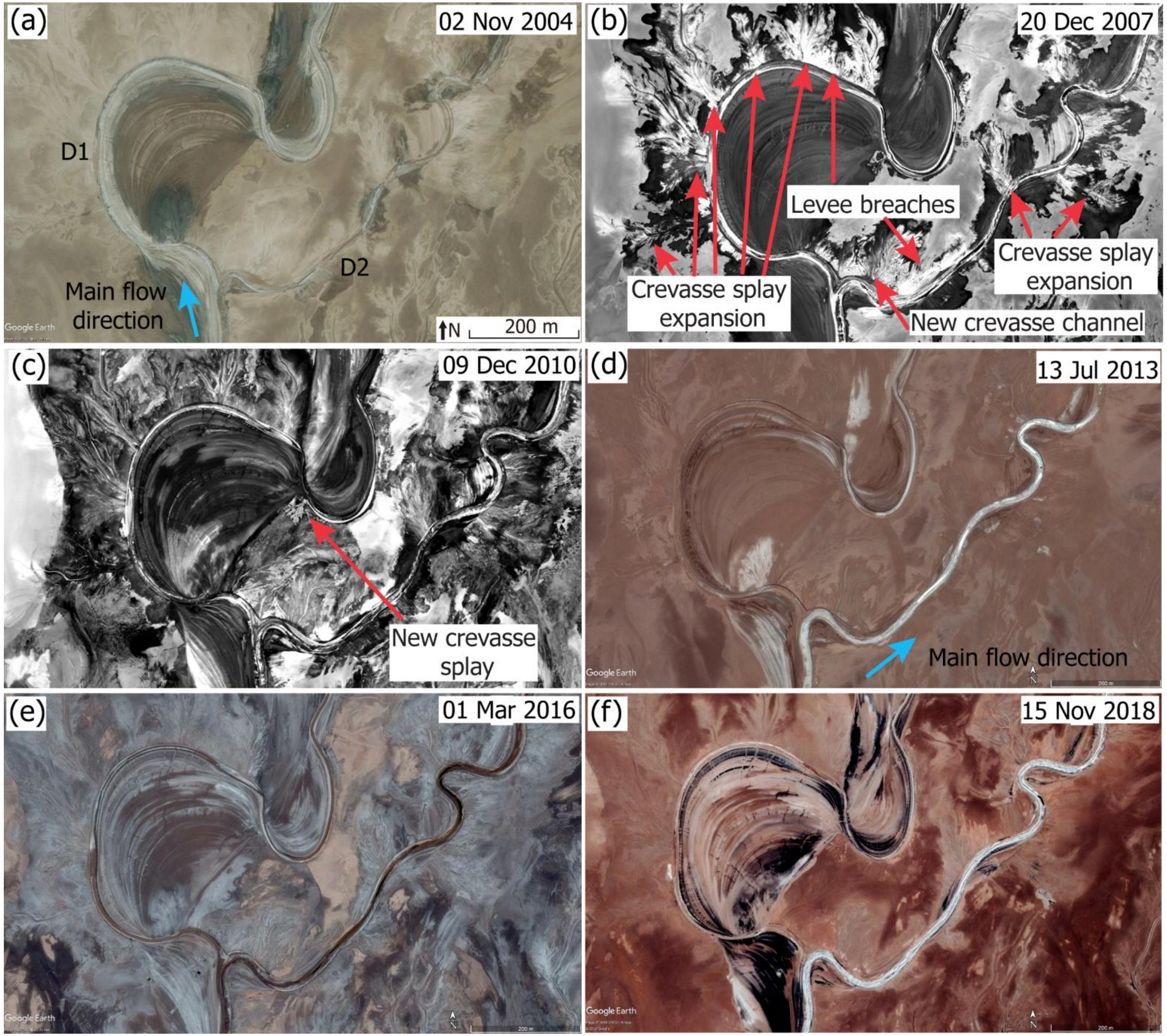

(a)
02 Nov 2004
D1
D2
Main flow direction
N
200 m
Google Earth
(b)
20 Dec 2007
Levee breaches
Crevasse splay expansion
Crevasse splay expansion
New crevasse channel
(c)
09 Dec 2010
New crevasse splay
(d)
13 Jul 2013
Main flow direction
Google Earth
(e)
01 Mar 2016
Google Earth
(f)
15 Nov 2018
Google Earth

Table 1

	Channel number	Mean width (m)	Mean channel depth (m)	Mean sinuosity index	Bankfull discharge (m^3/s)	Unit stream power (W/m^2)	Typical bed/bank sediment	Vegetation
Channels	C	36	1.3	1.19	99	<10	clay, silt, fine sand	No
	B	23	no data	1.37	46	<10	clay, silt, fine sand	
	D1	21.3	no data	1.41	42	<10	clay, silt	
	D2	21	no data	1.16	41	<10	clay, silt	
Floodplain		2234	-	-	-	-	-	No

Table 2

	Producer’s accuracy (%)	User’s accuracy (%)	Overall accuracy (%)	Kappa coefficient
Mean	91.68	97.33	93.09	0.84
Maximum	100	100	98	0.96
Minimum	79.31	92.86	86	0.72

Supplementary information

Visualisation of flooding along an unvegetated, ephemeral river using Google Earth Engine: implications for assessment of channel-floodplain dynamics in a time of rapid environmental change

Jiaguang Li[1*, 2], Stephen Tooth[3], Kun Zhang[4], Yang Zhao[1]

1 Key Laboratory of Tectonics and Petroleum Resources of the Ministry of Education, China University of Geosciences, Wuhan, 430074, China

2 Key Laboratory of Theory and Technology of Petroleum Exploration and Development in Hubei Province, Wuhan 430074, China

3 Department of Geography and Earth Sciences, Aberystwyth University, Aberystwyth, SY23 3DB, UK

4 Institute of Geological Survey of Qinghai Province, Xining, 810012, China

---

Correspondence: Key Laboratory of Tectonics and Petroleum Resources of the Ministry of Education, China University of Geosciences, Wuhan, 430074, China

Tel.: +86 27 67883067 fax: +86 27 67883051

E-mail address: jiaguangli@cug.edu.cn, jiaguangli@gmail.com (J. Li)

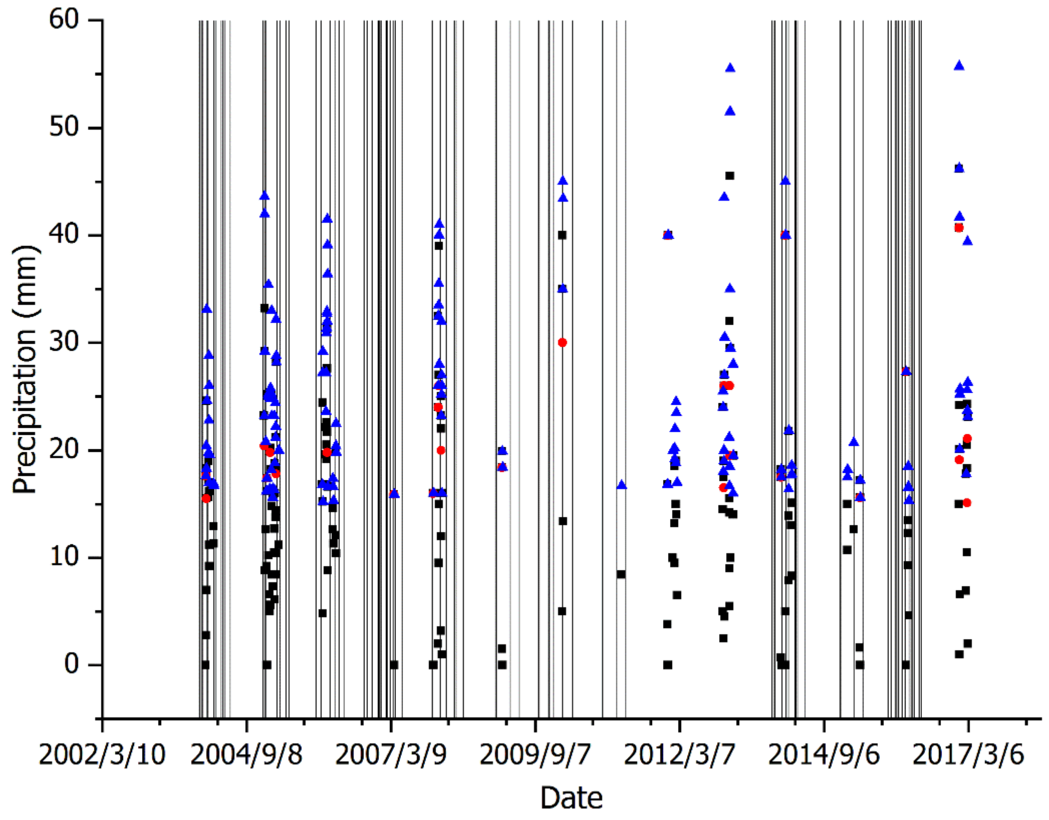

SI Fig. 1 Time series of available Landsat imagery and maximum precipitation datasets derived from daily precipitation: vertical lines indicate the timing of Landsat imagery used in this study; blue triangles are 3-day maximum precipitation; black rectangles are 2-day maximum precipitation; and red dots are yearly daily maximum precipitation.

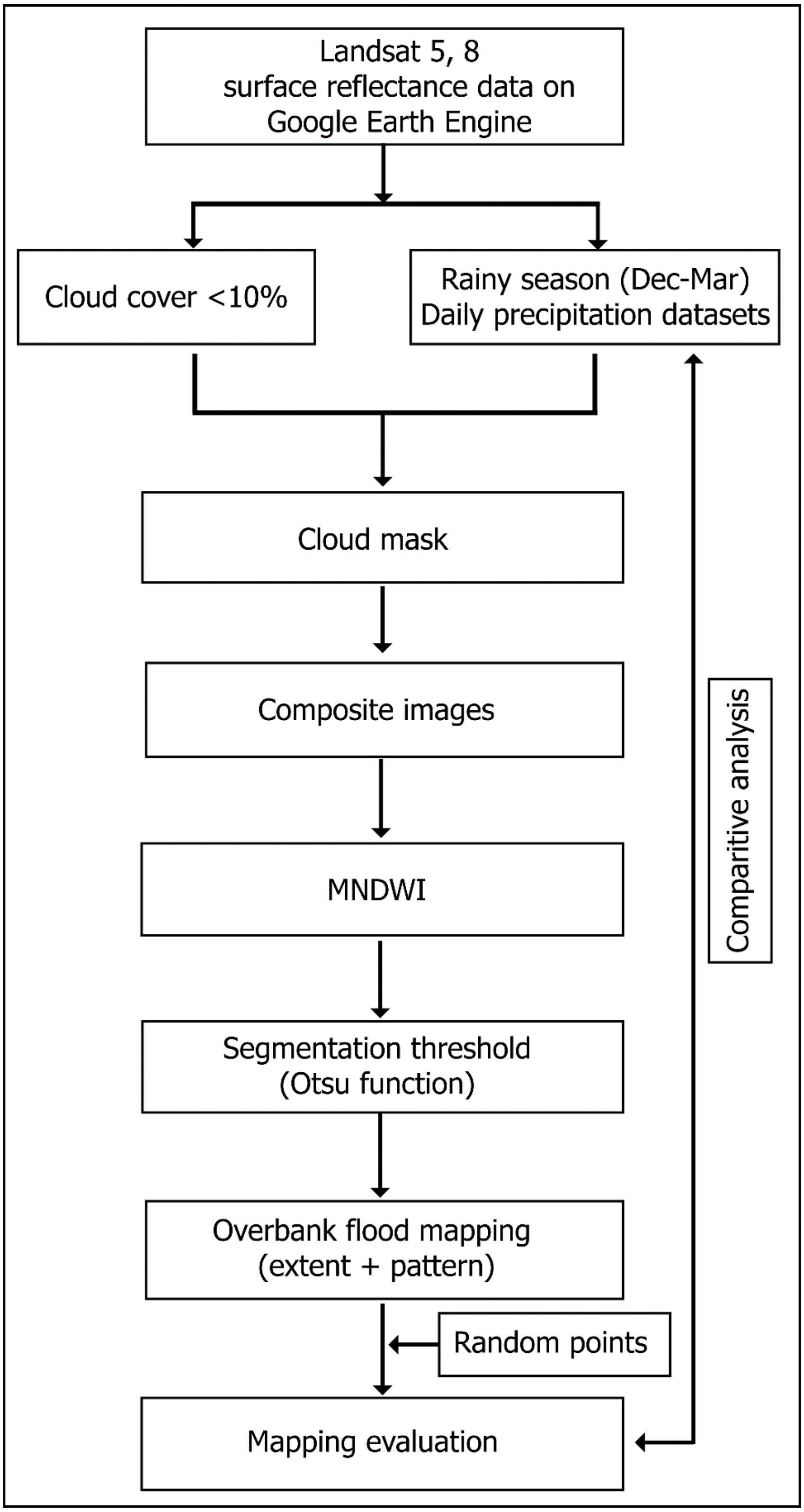

SI Fig. 2 Flow chart showing the procedure for mapping flood extent and pattern.

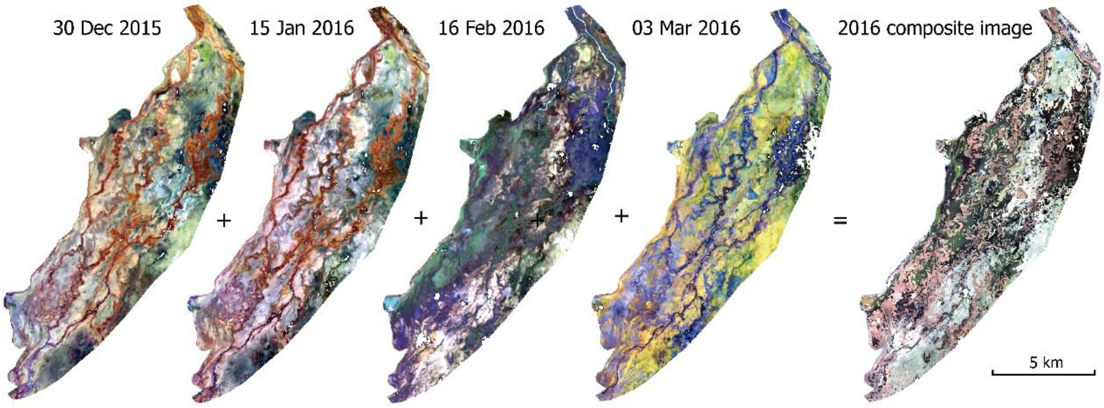

SI Fig. 3 Fig. 5 Example of a composite image derived from Landsat imagery for the 2016 (i.e. December 2015 through March 2016) rainy season. The images are presented as false colour images of bands 7 (red), 5 (green) and 1 (blue).

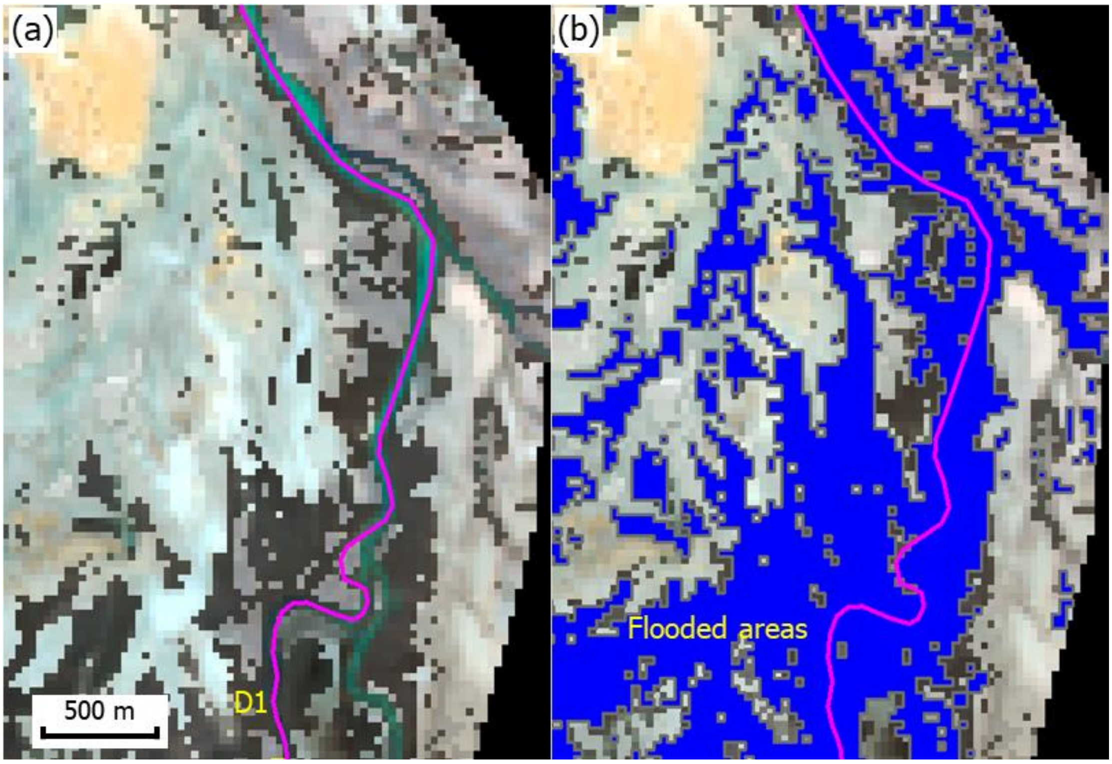

SI Fig. 4 Example of flood mapping along a secondary channel (D1) using a 2016 composite image: a) 2016 composite image; b) MNDWI-derived surface water areas (blue) in 2016.

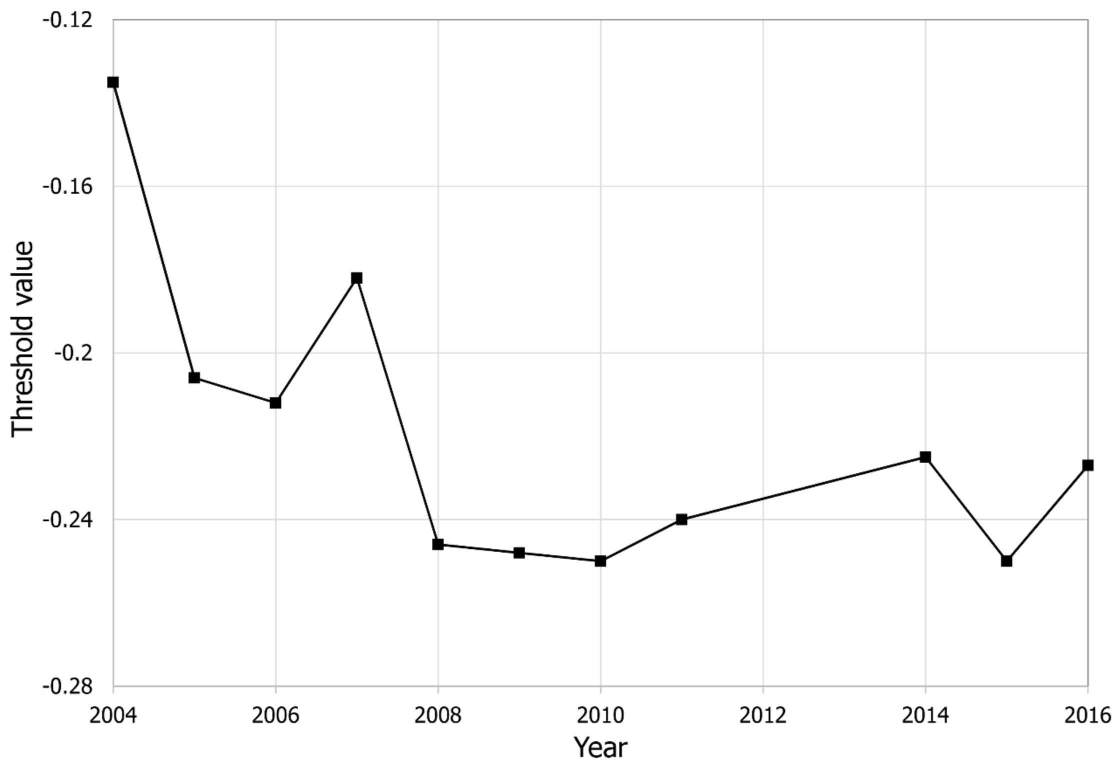

SI Fig. 5 Threshold demarcating flooded areas from dry land areas, as determined by Otsu's method.

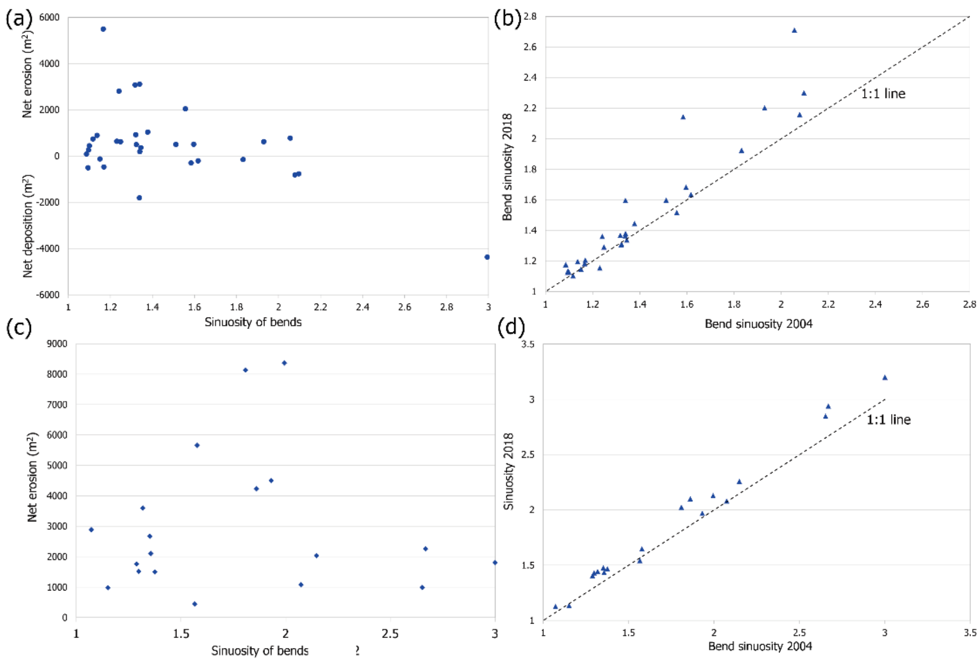

SI Fig. 6 Relationships between erosion/deposition and changes in sinuosity of individual channel bends for the years 2004 and 2018 along: a)-b) the trunk channel (reaches C-B);

and c)-d) a secondary channel D1.

SI Table 1 Number of Landsat scenes with cloud cover of <10% for the time period of interest. No Landsat data is available for the years 2012 and 2013.

Date	Year	Number of Scenes	Scenes			
Landsat 5	2004	3	30 Jan 2004	15 Feb 2004	18 Mar 2004	
	2005	2	05 Mar 2005	21 Mar 2005		
	2006	2	03 Feb 2006	08 Mar 2006		
	2007	4	05 Dec 2006	21 Dec 2006	22 Jan 2007	11 Mar 2007
	2008	2	10 Feb 2008	29 Mar 2008		
	2009	1	16 Mar 2009			
	2010	2	13 Dec 2009	15 Feb 2010		
	2011	1	17 Jan 2011			
Landsat 8	2014	3	24 Dec 2013	09 Jan 2014	26 Feb 2014	
	2015	1	01 Mar 2015			
	2016	4	30 Dec 2015	15 Jan 2016	15 Feb 2016	03 Mar 2016

SI Table 2 Details of the high resolution satellite imagery used in this study

Type	Catalog ID	Acq. date	Avg. off nadir angle	Avg. target azimuth	Sensor	Dataset types
Quick Bird-02 (GoogleEarth)	10100100035DE200	02 Nov 2004	8°	293°	QB02	Surface reflectance
Worldview-02	1020010001455700	30 Dec 2007	17°	85°	WV01	
	10300100084D5600	09 Dec 2010	13°	173°	WV02	
Pléiades	DS_PHR1B_201307131443591_SE1_PX_W067S21_0310_02391	13 Jul 2013	16°	33°	PHR1B	
	DS_PHR1B_201603011443021_FR1_PX_W067S21_0310_02408	01 Mar 2016	11°	69°	PHR1B	
	DS_PHR1A_201811151436194_FR1_PX_W067S21_0207_01728	15 Nov 2018	20°	89°	PHR1A	